10.48047/jocaaa.2024.32.01.72

PET Detector Modules Based on Detector Crystal Technologies

Rahul P. Mahajan
Research and Development Department
Healthcare and Medical Device Development Industry
College of Engineering
Pune, India
rpm.mahajan@gmail.com
0009-0003-3038-4391

***Abstract*—The diagnosis of neurological disorders, circulatory system disorders, and tumors is frequently accomplished using Positron Emission Tomography (PET). An essential component of PET scanners are scintillation crystals, which can transform γ photons into fluorescent ones in order to determine their energy, location, and time. Currently, identifying scintillation crystals with improved performance is a key research objective in PET. Different scintillator materials (LYSO (Lutetium-Yttrium Ox orthosilicate), LSO (Lutetium Ox orthosilicate), GAGG (Gadolinium Aluminum Gallium Garnet), BGO (Bismuth Germinate), $BaSO_4$ (Barium Sulphate), crystal geometries (cuboid, pixelated, monolithic, dual-layer), and surface treatments are utilized in this research to evaluate the efficacy of PET detectors. The major things that are looked at are Energy Resolution (ER), Depth-of-Interaction (DOI), and Coincidence Time Resolution (CTR). LYSO cuboid crystals achieved the best CTR of 107 ps and ER of 11.57%. GAGG cuboids showed superior ER of 8.58% with CTR of 114 ps. Dual-layer LYSO crystals (3× 3× (8+12) mm^3) reached CTR of 274 ps and ER of 13.9%. DOI resolution was highest for fine-pixel LYSO (1×1×20 mm^3) at 2.33 mm. Polished BGO arrays performed poorly with 18.4 mm DOI. Results show that pixelated LYSO and GAGG arrays provide the best combination of timing, energy, and depth resolution. Surface treatments and crystal geometry significantly influence performance. These findings guide the design of high-resolution, time-of-flight PET systems for clinical and research applications.**

***Keywords*—Medical Imaging, PET Detector Modules, Scintillator Crystals, Coincidence Time Resolution (CTR), Detector Module, LYSO Crystals, Spatial Resolution.**

I. INTRODUCTION

In recent decades, the discipline of medical imaging has advanced rapidly, revolutionizing the way diseases are diagnosed, monitored, and managed. These technological developments have significantly improved the ability to visualize both anatomical structures and physiological processes, offering clinicians powerful tools for early and accurate diagnosis. PET, or Positron Emission Tomography is one of the many ways to take pictures, is notable for its exceptional capacity to deliver functional and molecular-level data, which is essential for comprehending the underlying biology of diseases. In contrast to structural imaging methods that show anatomical features, such PET, CT (computed tomography), or MRI (magnetic resonance imaging) focuses on detecting changes in biochemical activity, often identifying disease before structural alterations become apparent. This functional sensitivity has made PET a vital tool in oncology, neurology, and cardiology, where early detection, staging, and therapy monitoring are crucial. As clinical applications continue to expand, the demand for higher-resolution and more sensitive PET imaging systems has become increasingly important—especially for targeting smaller organs or subtle pathological changes.

Meeting this demand requires innovation at the core of PET system design: the detector module. The primary function of the 511 keV gamma photons released during positron annihilation events in the body is to be detected by this module. These detections form the raw data from which PET images are reconstructed, meaning that the quality of The detector components' performance has an immediate effect on the finished image [1]. Critical parameters like sensitivity and spatial resolution, timing precision, and particularly the selection and design of the detector crystal technology have a direct impact on the gamma photons' depth of interaction (DOI) [2]. Traditionally, PET systems have employed pixelated scintillation crystals, arranged in arrays and coupled with photodetectors to estimate the location of photon interactions. While this configuration has served well for conventional whole-body imaging, it presents significant limitations particularly parallax errors and poor DOI resolution when imaging small structures or when photons enter the crystal at oblique angles. These limitations not only degrade image sharpness and accuracy but also restrict the potential of PET in high-precision applications such as brain imaging, breast cancer detection, and cardiac studies.

To overcome these constraints, research has increasingly turned toward scintillator crystals, which offer a continuous detection volume rather than discrete segments. This continuous structure allows for more accurate reconstruction of the interaction point by analyzing the distribution of scintillation light across the crystal surface [3]. When combined with advanced signal processing algorithms and high-performance photodetectors, such as Silicon Photomultipliers (SiPMs), monolithic detectors can offer enhanced spatial resolution, improved DOI estimation, and increased system sensitivity. These benefits make them especially well-suited for the creation of PET systems of the future, including compact, organ-specific scanners that demand high resolution within a limited field of view. As PET imaging continues to evolve toward greater precision and versatility, the choice between pixelated and monolithic scintillator crystal technologies has become a central consideration in system design. Each approach brings distinct benefits and compromises pertaining to manufacturing complexity, cost, resolution, and DOI capabilities, all of which have an impact on the PET scanner's total imaging performance and clinical usefulness.

A. Motivation and Contribution

The increasing demand for Advanced detector modules are being developed in response to the importance of PET imaging with excellent sensitivity and resolution for use in both animal studies and human clinical trials. Even though

10.48047/jocaaa.2024.32.01.72

scintillator-based PET detectors have come a long way in the last few years, current designs are still hampered by problems with depth-of-interaction (DOI) validation, coincidence time resolution (CTR > 500 ps), and scalability, calibration, and cost-effectiveness. Furthermore, although alternative scintillator materials exhibit superior timing and DOI characteristics, most systems rely on LYSO, leaving potential performance improvements unexplored. This work addresses these challenges by aiming to develop a unified PET detector architecture capable of achieving CTR, Energy resolution (ER) and DOI resolution while maintaining modularity, computational efficiency, and practical feasibility for both clinical and brainPET systems. The main contribution of this paper are as:

- Seamless integration of Monte Carlo (GATE/GEANT4) modeling with real-world prototypes ensures accurate prediction and validation of detector behavior.
- The study identifies pixelated LYSO and GAGG arrays as next-generation solutions, offering an ideal balance of timing precision and energy discrimination for high-resolution, time-of-flight PET imaging.
- Evaluation of geometry-dependent effects (cuboid, elongated, pixelated, dual-layer) on CTR, ER, and DOI resolution.
- A comparative performance analysis of multiple scintillator technologies, highlighting trade-offs between timing precision (CTR) and spectral accuracy (ER).

Despite significant advances in PET detector modules, current designs still face limitations in simultaneously achieving high timing accuracy, energy resolution, and depth-of-interaction precision. Most systems rely on conventional LYSO crystals, while alternative scintillator materials with superior properties remain underexplored. High-resolution modules often encounter reduced packing efficiency, calibration complexity, and increased computational overhead, hindering practical scalability. This study is justified in addressing these challenges by exploring a modular detector architecture that combines optimized scintillator surfaces, reflective coatings, and advanced readout strategies such as neural-network-based or light-guided decoding. The novelty of this work lies in proposing a scalable, cost-effective PET detector module design that improves overall performance while simplifying integration for clinical and brain imaging applications.

B. Outline of the Paper

The paper has the following structure: Section II introduces medical imaging and Section III present the PET, and their factors and properties. Section IV presents the principle of PET imaging, while Section V provides the PET image segmentation. Section VI introduces PET detector modules, and operational principles. Section VII presents a literature review of recent PET detector studies using crystal technology. Section VIII presents the method and material, analysis, and comparison are presented in Section IX. Section X has the conclusion, which sums up the results and talks about what needs to be done next.

II. MEDICAL IMAGING: AN OVERVIEW

The ability to visualize a subject's internal structures and/or the physiological processes that are concealed behind the skin makes medical imaging crucial to clinical analysis and illness diagnosis. Additionally, medical imaging aids in the creation of a database including thousands of physiological and anatomical images. These databases have developed into an effective teaching tool for physicians and new machine-based techniques to detect anomalies. All non-invasive medical imaging techniques allow the physician to use technology that can see into the patient to diagnose and treat a variety of illnesses. There are two kinds of information that a physician might want in medical imaging. These are the physiological and activity functions of the organ being studied, or its anatomical structure. Public health, which is of interest to everybody, is the common aim of the incredibly rich ecosystem that is medical imaging, which connects many different specialties. In such an environment, physicians exchange information with engineers, bioengineers, and other medical professionals, advancing the technology that enables early disease diagnosis or the tracking of new research to obtain a better understanding of how the human body functions.

A field of imaging methods, including PET, have been used in the medical imaging area [4], the most prominent of which are optical coherent tomography (OCT), single photon emission computed tomography (SPECT), magnetic resonance imaging (MRI) [5], ultrasonic imaging (UI), and X-ray computed tomography (CT). Among these imaging methods, the exceptional sensitivity of PET to changes in molecular-level metabolic and biological activities has made it one of the most effective methods for obtaining functional images. PET is now being employed in many different therapeutic domains, including neurology for Oncology for the identification and staging of cancer or tumours, cardiology for coronary artery disease and myocardial viability assessment, and Alzheimer's disease and mobility issues [6]. PET has also grown in importance in preclinical applications in recent years, when illness is studied and novel medication development and treatment approaches are tested using animal models rather than human ones. Although tiny rodents are the primary target of animal PET imaging, investigations on primates have also been conducted because of their significant genetic similarity to humans. PET, Molecular imaging allows researchers to analyses the metabolic and biological processes of study participants without invasively entering their bodies, which is particularly helpful when working with animal models. For preclinical applications, several animal PET scanners have been created as a consequence [7].

A. Structural And Functional Imaging

The anatomical makeup of the patient's tissues and skeletal information can be obtained through the use of structural imaging methods. Conversely, functional imaging methods enable the monitoring of physiological processes within the patient's body, including organ blood flow and heart pump activity. Medical imaging techniques are hard to categorise neatly into structural or functional categories these days. The imaging strategy of medical research dictates whether a certain modality is structural or functional. The first imaging medium utilised in medicine was X-ray planar imaging. Similar to any imaging system, a point on the image sensor

10.48047/jocaaa.2024.32.01.72

and a point in the object to be evaluated must coincide exactly (see Figure 1). Using a point-like X-ray source allows for this relationship in clinical X-ray planar imaging. Due to the X-ray's ability to penetrate deeply, this image modality operates in transmission mode, allowing for the imaging of the body's internal structure.

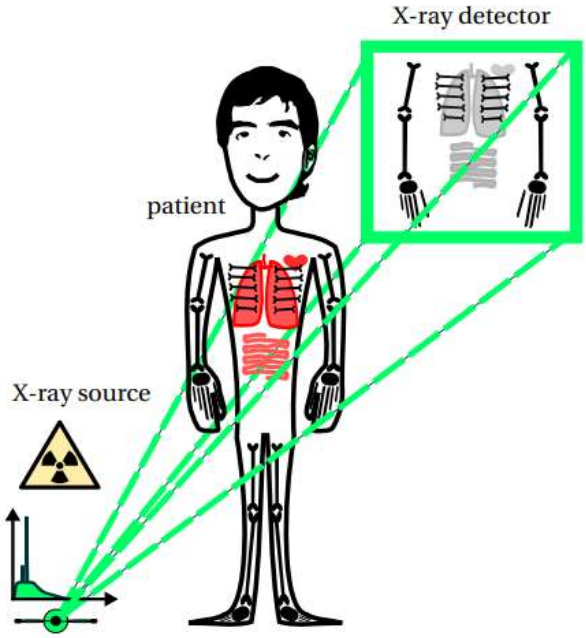

Fig. 1. The technique of making a planar X-ray image.

The patient lies between a revolving X-ray source in a clinical X-ray CT scan and a detector array to acquire projection data, from which 3D images are reconstructed (Figure 2).

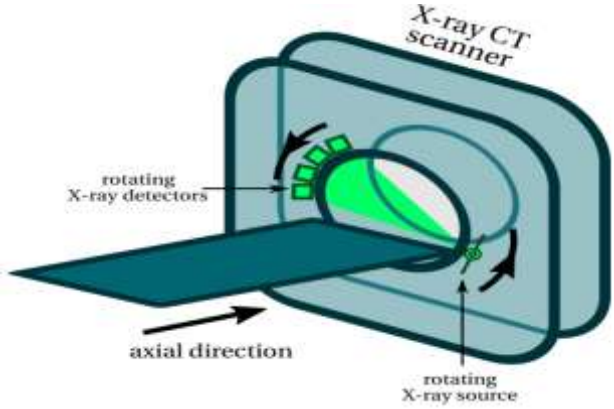

Fig. 2. A diagram of a system for rotating X-ray computed tomography.

With continuous bed movement, axial or helical scanning can produce whole-body volumetric imaging. Due to limited contrast in soft tissues, CT is mainly applied for structural assessment, such as lesion detection, trauma evaluation, and cardiac infarct size estimation. In comparison, MRI relies on nuclear magnetic resonance, using strong magnetic fields and gradient coils for selective excitation and detection [8]. MRI is appropriate for musculoskeletal research because it offers superior soft-tissue contrast, and it is also widely used in functional brain imaging.

B. Molecular Imaging

Since the middle of the 1990s, the field of molecular imaging has developed a suite of techniques and instruments that, via the use of certain molecular probes, enable the visualization and assessment of cellular and molecular biological activities that take place in vivo. Molecular imaging makes it possible to see the distributions of molecular probes in both space and time. These probes have been designed to target certain biological activities [9]. Because physiological and cellular processes are closely related, functional and molecular imaging are also closely related. The primary distinction, though, is found in Molecular imaging is to observe biological processes with the required molecular sensitivity. The image contrast enhancers used in molecular imaging are called molecular probes. New molecular probes have been developed in large part thanks to nuclear medicine, and small-animal PET imaging in particular. The first prerequisite for any imaging modality capable of performing molecular imaging is the presence of sufficient molecular sensitivity. Here is an explanation of a general example of molecular medical research to help qualitatively comprehend the compromises related to a certain visual modality's molecular sensitivity:

- A molecular probe is first administered to the patient, and it is then waited for sufficient probe accumulation in a target lesion.
- The patient is next given an X-ray CT scan, which yields a structural image. The whole structural tomographic analysis is shown in an axial slice in Figure 3.
- Lastly, the patient is shown a combination of a molecular imaging method that looks at and estimates the spatial and/or temporal distributions of the molecular probe that was given, and an axial slice of the molecular tomographic analysis.

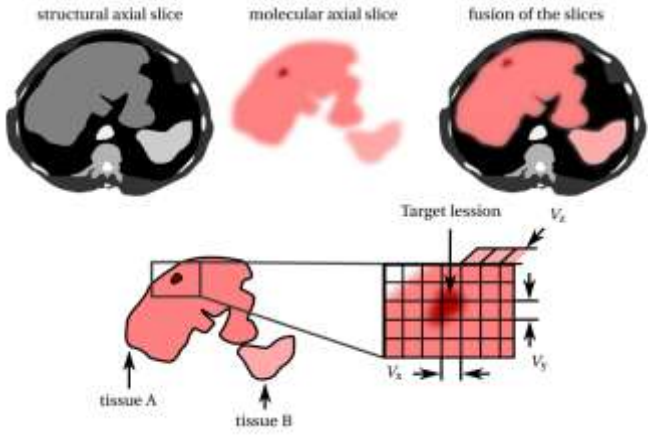

Fig. 3. Representation of the molecular imaging study example.

This scenario would be similar to a PET/X-ray CT investigation, where a PET scanner measures the distribution of molecular probes and a CT scanner estimates the structural information. A portion of the molecular probe that is administered makes it to the intended lesion, while the remainder is absorbed by tissues A and B, adding unwanted background counts. The imaging apparatus itself introduces noise counts in addition to the a specific probe background, and these may rise based on the dispersion of the a specific probe.

10.48047/jocaaa.2024.32.01.72

III. Positron Emission Tomography (PET)

As a form of emission-mode tomography, the patient generates the signals that are shown in Figures 4, the PET scanner does not act as a barrier between the source and the detection system, but rather picks up. The detection of electron-positron annihilations using electronic collimation is another crucial component of PET. PET involves giving the patient a molecular probe labelled with a positron-emitting radioisotope, such as Cu-labeled copper(II) pyruvaldehyde bis (N-methylthiosemicarbazone), Cu(PTSM), or F-fludeoxyglucose, F-FDG. In a PET examination conducted for oncology purposes, Cancer cells are identified using the provided molecular probe, usually F-FDG, since they absorb abnormally high quantities of the protein. PET is a unique imaging modality for tumor identification because to its great molecular sensitivity, which means that no other imaging modality in this sector can replace it.

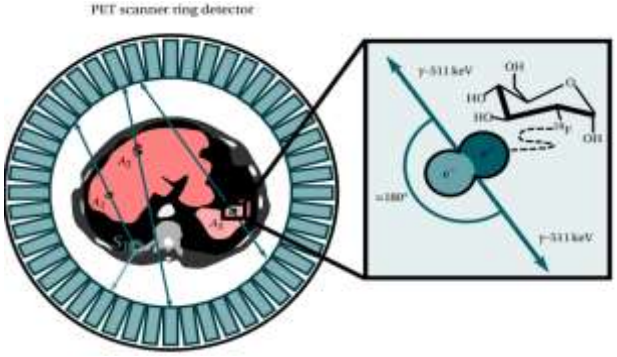

Fig. 4. A diagram that shows how PET works[10]

The β^+ decay of the positron generated by the 18F radioisotope in F-FDG traverses a limited distance (the positron range) prior to merging with an electron to create positronium. Annihilation takes place after hundreds of picoseconds, resulting in two consecutive 511 keV γ-photons. PET detects these photons without a physical collimator (electronic collimation), unlike SPECT, which requires a high-density collimator due to noncollinear low-energy γ-photons, reducing sensitivity. In PET, SPECT, and CT, volumetric images are reconstructed from projection data: CT measures X-ray attenuation, while PET/SPECT measure molecular-probe concentration. Compton scattering can cause photon energy loss and trajectory deviation, affecting detection.

A. The Fundamentals of PET Detectors

The detection technique used to describe the entering annihilation photons can be broadly classified into two types: direct and indirect. Photoelectric or Compton scatter interactions are the means by which each incoming annihilation photon interacts with the scintillation crystal in indirect (scintillation) detection. Before being transformed into an electrical current by one or more photodetectors, the deposited energy is first transformed into a stream of visible (lower-energy) light photons. Every PET system now on the market uses this detection technique (2). Using semiconductor crystals, every interaction between incoming photons is instantly transformed into electrical impulses via direct detection. This strategy has only been investigated in studies thus far [11][12]. Every one of these approaches has unique benefits and drawbacks.

1) Method of Indirect Detection (Scintillation)

Scintillation detectors for PET use an inorganic crystal, which each entering 511-keV annihilation photon reacts with (by Compton scatter or the photoelectric effect), producing a swiftly expelled recoil electron. Through coulombic interactions, each ejected electron passes through the material and ionizes it, releasing a trail of secondary electrons (5) from the inherent electrical valence band of the crystal into the conduction band. The resulting ionization charge is transformed into a flash of isotropically produced visible light (6) by a subsequent deexcitation process in which those excited electrons fall into accessible energy levels of the host crystal or those of an impurity added to the crystal. A photodetector element connected to the crystal gathers light and transforms it into an electrical signal, which is then processed by readout electronics (7).

2) Inorganic Scintillation Crystals Used in PET

In order to achieve adequate coincidence timing resolution, ideal inorganic scintillation materials should have a high density and effective atomic number (Zeff). The resultant signals should also have a fast rise and decay duration. With the exception of a few intrinsic scintillators like bismuth germanium oxide (BGO), a tiny concentration of an impurity known as an activator is added to the inorganic scintillation crystal (8) in order to encourage the production of visible-light photons, or optical photons. An overview of PET detector types is given in Table I:

TABLE I. Overview of PET Detector Types and Scintillation Principles.

Category	Description / Working Principle	Key Characteristics	Examples / Notes
Indirect Detection (Identification of Scintillation)	Photoelectric or Compton scatter interactions are used to interact with each incoming 511-keV annihilation photon inside a scintillation crystal. Photons of visible light are created from the deposited energy, and photodetectors are used to turn them into electrical impulses.	- Used in all current commercial PET systems. - Involves conversion from gamma photons → visible light → electrical signal. - Relies on scintillation crystals and photodetectors (e.g., PMTs, SiPMs).	Established method in PET imaging; offers mature technology and stable performance.
Direct Detection (Semiconductor Detection)	Without a light emission stage in between, semiconductor crystals transform incoming photons straight into electrical impulses.	- Provides potential for improved spatial and energy resolution. - Currently limited to research due to complexity and cost.	Experimental stage only; examples include CdTe and CZT detectors.
Scintillation Process in Indirect Detection	A rebound electron is ejected by a 511 keV photon interacting through the photoelectric effect or Compton scatter. The crystal is ionised by the electron, creating secondary electrons. Their deexcitation produces isotropically emitted visible light photons,	- Involves ionization and deexcitation within the crystal lattice. - Produces a flash of visible light proportional to energy deposited. - Coupled with readout electronics for signal processing.	Common in BGO, LSO, LYSO, and GAGG crystals.

10.48047/jocaaa.2024.32.01.72

	which are then detected by photodetectors and processed electronically.		
Inorganic Scintillation Crystals in PET	To guarantee effective photon detection and adequate timing resolution, inorganic crystals with high effective atomic number (Z_eff) and density are favoured. Activator impurities are added to enhance light emission, except in intrinsic scintillators like BGO.	- High Z_eff and density improve photon stopping power. - For coincidence timing resolution, quick rise and decay times are essential. - Activators encourage the emission of visible light.	- High Z_eff and density improve photon stopping power. - For coincidence timing resolution, quick rise and decay times are essential. - Activators promote visible light emission.

B. Important Elements Affecting PET Imaging's Spatial Resolution

The detection of simultaneous 511 keV photon pairs produced by positron-electron annihilation is the basis of positron emission tomography (PET). After a brief journey through tissue, Ae^+, which is released by a radioactive tracer, interacts with a nearby e^- in order to trigger a catastrophic catastrophe. This process produces two 511 keV photons that are released 180 degrees apart and in opposite directions. The detectors pick up on these photons at precisely the right times, and each occurrence is given the appropriate line of response (LOR). Tomographic reconstruction of the tracer dispersion in three dimensions is made possible by aggregating several such occurrences that are situated on the LORs of the system. Technological and physical factors, including photon detection, annihilation, and E^+ emission, affect the reconstructed PET image's overall spatial resolution.

A PET system's spatial resolution depends on both design-dependent and intrinsic parameters. The annihilation photons' non-collinearity and positron range are inherent restrictions, while design-dependent aspects involve detector module design (crystal type, size, and geometry), photon penetration and parallax error, Compton scattering, patient motion, event position decoding, and image reconstruction methods. Scintillators like LSO, BGO, and GSO are commonly used, with properties such as light yield and decay time influencing performance. Overall, PET resolution reflects the combined effects of detector technology, system design, and unavoidable physical constraints.

1) Annihilation Photon Accolinearity

Annihilation is the process by which an electron (e) and a positron (e+) combine to produce two photons, each travelling in nearly opposing directions and having an energy of 511 keV. But the centre of mass of the positron and electron has kinetic energy because of the remaining initial inertia at the time of annihilation. As a result of this potential motion, the two 511 keV photons' ideal 180° emission angle is slightly off [13]. This angular deviation causes Gaussian blurring in a PET scanner with a circular or cylindrical geometry and a radius R, with an estimated FWHM of around 0.0044 R; Figure 5 provides a schematic illustration.

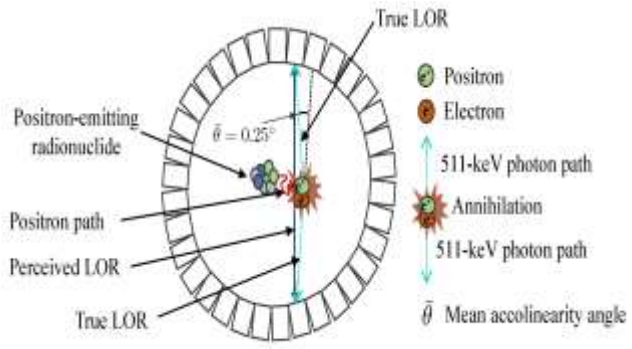

Fig. 5. The influence of non-collinearity in a PET scanner

The annihilation photon non-collinearity brought on by the kinetic energy that remains of the positron-electron pair's centre of mass at in reference to the re-created pictures, which are represented by 0.0044 R FWHM, where R is the PET scanner's cylindrical geometry's radius, there is an approximate Gaussian-shaped blurring caused by the point of annihilation.

2) Positron Range

A positron (e^+) in prior to encountering an electron (e^-) and destroying itself, the human body must travel a specific distance. This leads to a displacement known as the positron range between the annihilation site and the radionuclide's initial position. This issue leads to localisation mistakes when PET images are being reconstructed. How much blurring occurs is dependent on the positron's energy and the tissue's characteristics. Several radionuclides' positron ranges in water-equivalent media are shown in Table II.

TABLE II. POSITRON RANGE OF VARIOUS ISOTOPES IN WATER-EQUIVALENT TISSUE

Isotope	Half-Life	E_{mean} (MeV)	R_{mean} (mm)	R_{max} (mm)
^{18}F	110 min	0.250	0.6	2.4
^{15}O	2 min	0.735	3	8.4
^{11}C	20.4 min	0.386	1.2	4.2
^{13}N	10.0 min	0.492	1.8	5.5
^{64}Cu	12.7 h	0.278	0.7	2.5
^{89}Zr	78.4 h	0.396	1.3	3.8

3) Width of Detector Element

The spatial resolution of a PET scanner is significantly influenced by the detector element's diameter as well [14]. The larger crystal elements utilized to construct the PET ring's detector arrays lower the resulting images' spatial resolution, which in turn raises the uncertainty in pinpointing the system's 511-keV photon interaction sites. Figure 6 illustrates how the system's spatial resolution is impacted by scintillation crystal width.

10.48047/jocaaa.2024.32.01.72

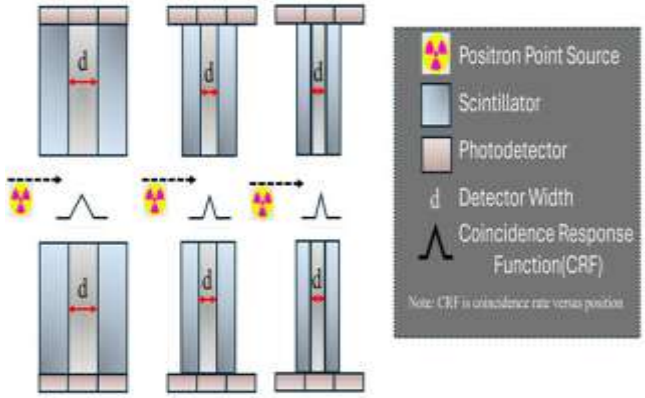

Fig. 6. PET scanner's detector element width in relation to spatial resolution.

The theoretical resolution limit is the least separable distance (d/2 FWHM) between two point sources. Although it enhances resolution, reducing detector width poses technical hurdles.

4) Design Techniques for PET Detectors with Ultra-High Spatial Resolution

PET resolution is limited by intrinsic characteristics, such is non-collinearity and the positron envelope, however, design improvements can enhance performance. Reducing scintillation crystal size improves spatial resolution but increases photodetector channels, inter-crystal scatter, and readout complexity. Electronic and optical multiplexing can make designs simpler and lower costs, but may affect energy, timing, and spatial accuracy. Other challenges include crystal scatter, photon penetration, and lack of depth-of-interaction (DOI) information, which cause image blurring. High-resolution PET benefits from high light-yield crystals, precise 3D event localization, and one-to-one photodetector coupling, though this raises costs and complexity. Balanced multiplexing offers a practical trade-off between resolution and system feasibility.

5) PET Detector Design with Advanced Photon Depth-of-Interaction (DOI) Capability

Several PET detector designs enable depth-of-interaction (DOI) measurement. Dual-end readouts use photodetectors at both ends of narrow crystals for DOI, but double the detector count, while single-ended readouts rely on light-sharing across detectors, achieving ∼2–3 mm DOI accuracy with fewer detectors [15][16]. A side-readout approach with an edge-on 8×8 LYSO array coupled to Position-sensitive avalanche photodiodes (PSAPDs) enables around ∼10% energy resolution and ∼1 mm DOI resolution. This design improves light collection uniformity, crystal packing density, and efficiency, offering high-resolution PET imaging in a compact configuration [17].

6) Image Reconstruction

Image reconstruction critically affects PET spatial resolution by converting raw coincidence data into radiotracer distribution maps. Resolution can be reduced by smoothing filters, which suppress noise but blur fine details, and by insufficient sampling, which causes aliasing [18]. Advanced algorithms, OSEM using point spread function (PSF) modelling, for example, can improve resolution by compensating for system flaws and detector blurring. But too much resolution recovery can magnify noise and produce artefacts, therefore it's important to carefully balance signal-to-noise ratio and image clarity.

C. Properties of Scintillation Materials

The requirements of the actual application determine the scintillator material selection. Numerous factors define the ideal scintillator:

1) Radiation Absorption Efficiency

The scintillators' ability to this parameter specifies the amount of radiation that may be absorbed during the scintillation conversion process. Further attention should be paid to radiation from the scintillator's optical spectrum. Because of a non-radiative process, the released photons are reabsorbed and eventually lost.

2) Light Yield (LY)

Light yield is the quantity of photons released for each unit of energy deposited, according to experts. When assessing scintillators' energy resolution, sensitivity, and efficiency, this is an essential consideration. The scintillating substance and the incoming photon interact to produce electron energy exchanges, which are primarily responsible for the production of light. Internal scattering losses might happen as the photons reabsorb after the light has been emitted. It's possible that the average scintillation light production is less than what is predicted mathematically.

3) The ability to discriminate between pulse shapes

Neutron-gamma (n-γ) pulse discrimination is well recognised and has been applied in a variety of organic scintillation materials. In a scintillator, the light output is the energy, expressed in eV, that one electron needs to generate a pulse with an equivalent light output. The recoil protons produced by hydrogen usually create significantly smaller pulses as opposed to secondary gamma-ray electrons produced by elastic scattering with the same energy. The PSD approach is commonly used in organic scintillators for n-γ discrimination, or the separation of recoil protons generated by neutron interactions from Compton electrons emitted by gamma rays.

4) Emission Wavelength

The photo-detector spectra and scintillation emission spectra should coincide to prevent post-scintillation losses. This is known as "spectral matching." It is frequently more an engineering than a material issue to require that where the scintillator produces light is where the sensitivity and efficiency of the detector are at their maximum.

5) Response Time

Organic scintillation detectors provide a high temporal resolution, which is especially useful for high-energy neutron and gamma-source studies. The scintillation's decay period is used to calculate the response time. The neutrons inside the detector, however, make the temporal response in neutron detection particularly noteworthy. Fast reaction times are crucial for timing-sensitive applications, such as computer tomography and accelerator particle detection. The primary drawback of these uses includes certain scintillators undergo an extra trapping stage before lighting, often known as afterglow. Certain quenching procedures may affect the scintillators' light production efficiency. Because Intensity discrimination may be affected by the radiation's linear dependence on the scintillation response.

10.48047/jocaaa.2024.32.01.72

6) Energy Resolution

The energy resolution can be calculated by dividing the full width at half maximum (FWHM) of the excitation energy by the peak energy of the pulse height spectrum. The apparent non-proportionality of scintillators' light output is one of the primary downsides of energy resolution. For the majority of scintillation detector applications, good ER is crucial. The summary of properties is provided in Table III.

TABLE III. THE PROPERTIES OF SCINTILLATION MATERIALS

Property	Description	Significance / Application	Limitations / Considerations
Radiation Absorption Efficiency	Effectiveness of scintillator in absorbing radiation; considers optical propagation and self-absorption	Determines how well the scintillator converts radiation to detectable photons	High self-absorption leads to photon loss via non-radiative processes
Light Yield (LY)	Number of photons released for every energy unit put	Crucial for sensitivity, efficiency, and energy resolution	May be lower than theoretical due to internal scattering and reabsorption
Shape Discrimination in Pulses (PSD)	Ability to distinguish neutron vs gamma interactions (n-γ discrimination)	Important in neutron detection and radiation monitoring	Limited to certain materials; requires analysis of pulse height differences
Emission Wavelength	Wavelength of scintillation emission should match photodetector sensitivity	Ensures efficient photon detection and reduces post-scintillation loss	Mismatch between scintillator emission and photodetector sensitivity reduces efficiency
Response Time	Time taken for scintillator to emit light after radiation interaction	Critical for timing-sensitive applications like PET or particle detection	Afterglow and quenching processes can delay or reduce light output
Energy Resolution	Ratio of FWHM of pulse height spectrum to peak energy	Important for distinguishing different energy photons	Non-proportionality of light yield reduces resolution

IV. PET IMAGING PRINCIPLES IN NUCLEAR MEDICINE

The PET imaging approach utilizes radionuclide-labelled radio-pharmaceuticals to precisely identify and locate annihilation events that occur after beta-plus decay (Figure 7). It uses the necessary electronic signal and image-processing procedures when a photodetector recognizes the annihilation output gamma ray and a suitable device converts it into an acceptable electrical signal. By sorting the coincidences, a projection data or sinogram with information on the annihilation event is produced. To recreate the image in a tomographic fashion, these data are subjected to further processing using image reconstruction algorithms [19]. Because they can identify the site where the substance labelled with the radionuclide source has greater rates of absorption and consumption, radiotracers are biochemicals that have been radionuclide-labeled.

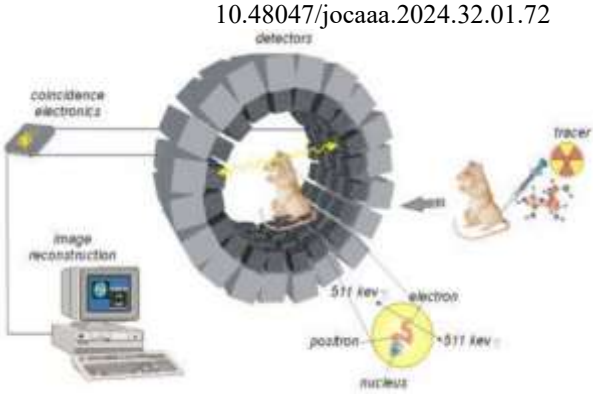

Fig. 7. PET imaging process schematic representation [20]

PET imaging often uses glucose radiotracers that are labelled with O, C, Na, and F for imaging purposes. This is because cancer cells need glucose more often than healthy tissue cells [21]. The distribution of glucose metabolism in the region can be determined by injecting radionuclide-labeled glucose and detecting the annihilation output gamma rays and their geometrical relationship. Two photons traversing 180 degrees are produced when a positron undergoes annihilation in beta pleat-plus decay. The pair formation radiation tissue contact mechanism states that us decay brings two photons back to one another in a 180-degree path. This is utilized in PET imaging to assist detect the annihilation event (Figure 8).

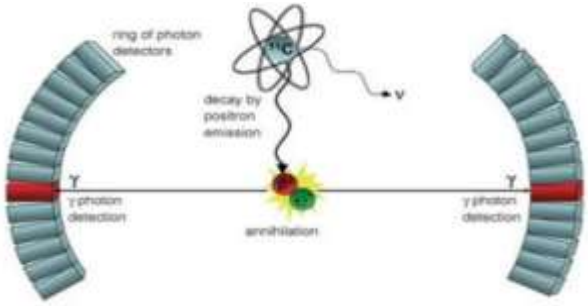

Fig. 8. Schematic representation of the principle

These photons fall into in the electromagnetic spectrum, the gamma-ray band and are released at an energy of 511 Kev. They could be detected outside the body due to their high energy spectrum, which prevented them from being absorbed by bodily tissue. In particular, positron annihilation point localization is accomplished by simultaneously detecting these photons using photodetectors positioned opposite one another [22].

A. Physical Challenges in Integrating PET and MRI

The design of PET-MRI is technically challenging due to the influence of strong magnetic fields, requiring integration without compromising either modality. Two main designs exist: sequential acquisition (Figure 9a), where PET and MRI are performed sequentially with co-registration software. This design, adopted by Philips as TF-PET/MRI, is economical, reduces claustrophobia, and minimizes magnetic interference, but suffers from motion artefacts and large space requirements (~4.3×13m). In contrast, simultaneous acquisition aims to embed both modalities within a common gantry, available since 2006 in two forms: PET insert in MRI (Figure 9b) and fully integrated systems (Figure 9c).

10.48047/jocaaa.2024.32.01.72

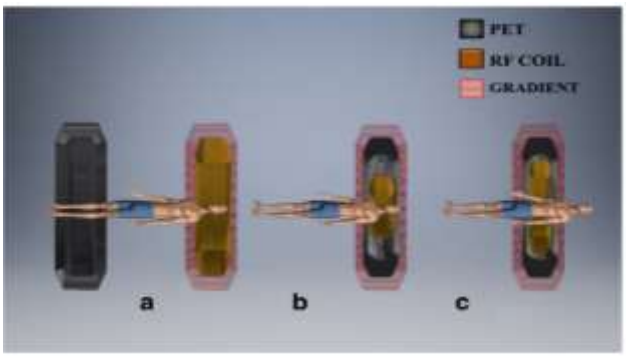

Fig. 9. A sequential design, a simultaneous PET insert MRI scanner, and a simultaneous completely integrated system are the three different PET/MRI designs

This tactic, which aims to lower the system's occupancy, is rather common. However, many technical issues pertaining to the system's compatibility should be resolved by the design. Let's talk about the physical difficulties in combining PET and MRI (Figure 10).

Fig. 10. Challenges in fusing PET and MRI

1) MRI system affecting PET

The primary goal is to get the high performance of both modalities without sacrificing each one, even if Physical interaction problems are caused by the block detectors' thickness and hole size in PET. The operation of PET has been affected by radiofrequency broadcasts, gradient magnetic fields, and extremely high static magnetic fields (see Table IV).

TABLE IV. MRI SYSTEM AFFECTING PET

MRI components	Effect on PET	Consequences	Resolution
Static magnetic field	Affects the trajectory of electron flow during readout	Reduced gain factor.	A solid-state photo detector (SSPD), such as a Silicon Photomultiplier (SiPM) or Avalanche Photodiode (APD), can be used in place of the photomultiplier.
Gradient magnetic field	Heats up the equipment	Mechanical vibrations and leading to vibrations.	Electrical component restructuring. eddy current induction. repairing the temperature control apparatus.
RF Interference	Introduces a noise signal.	Introduces eddy current as a result of magnetic induction. creates a heating effect.	Encircling the coil with an RF shield.

2) Static Magnetic Field

The abnormally elevated static magnetic field has interfered with the electron flow in Photo Multiplier Tubes (PMT), which makes up the block detectors that are part of the PET system's scintillator. Information is lost in a specific area as a result of the Lorentz force deflecting the electrons' path between the dynodes. As a result, steel or mu-metals must be used to protect the PMT tubes. Additionally, since the PMT only detects x-rays and gamma rays, it might be substituted with Light detectors that function better in the presence of magnetic fields, include optical fibers. However, the signal is attenuated due to the length of the optical fibers. To lessen its sensitivity to the strong magnetic field, the PMT might be swapped out with position-sensitive PMTs (PSPMT) and field-insensitive PMTs like Avalanche Photodiode (APD). APD is insensitive to a magnetic field and may be directly attached to 1-2 mm short light guide on a block detector's scintillator crystal, despite its reduced gain factor and extreme sensitivity to temperature changes.

3) Gradient Magnetic Field

In order to accomplish the greater depth of skin at lower frequencies, at a rate of 1 kHz, the gradient magnetic fields are quickly altered, creating eddy currents inside the PET circuitry. The electronics in the PET system heat up and vibrate mechanically when eddy currents are introduced. Therefore, copper or aluminium that is connected to the ground is intended to protect the high frequency electronics. Copper's non-magnetic and non-ferromagnetic properties allow it to offer around 99% electrical isolation around PET detector circuitry. The gradient sequence reduces the PET/MR system's sensitivity by 5–20%. The electronics that are located closer to the gradient coil, such as solid state photo detectors, must be extremely durable. If not, a modification of the PET readout mechanism is intended to reduce the oscillations.

4) Radio Frequency (RF) Signal

The MRI transmission coils generate radiofrequency signals that make the PET system's electronics vulnerable while the MRI is being acquired simultaneously. The high-frequency band is where this influence is most noticeable. SNR is decreased due to RF interference. By using conductive materials, such as copper, to insulate PET detectors, this issue may be avoided. Nevertheless, it causes eddy currents to circulate in the conductive shielding [23]. This indicates that it may alter. RF interference can be mitigated by "coupling-decoupling" the RF receiver coil with the clock frequencies and phase relationships of digital electronics. As a result, the RF field that is released may be adjusted to work with the MRI-RF coil's reduced field coupling. FPGA-based technology was used to perform the diSPM's frequency and phase switching, utilized by Hyperion IID PET's PET modules.

5) PET System Affecting MRI

10.48047/jocaaa.2024.32.01.72

The following parameters, on the other hand, also impact the magnetic properties of the MRI apparatus when PET detectors are included within the magnetic bore (see Table V).

TABLE V. PET SYSTEM AFFECTING MRI

Components of PET	Effect on MRI	Consequences	Resolution
Scintillator detector	Nonuniformity of the main magnetic field (B0)	Presents magnetic induction.	Changing to scintillation detectors that are compatible with MRI
Gamma Shielding	Introduction of distortion and nonlinearity induced by eddy currents	Higher cost	Alternative materials for shielding have been chosen
Electronics and PET cables	Reasons for radiofrequency interference	Heating effect	The addition of an RF shield to PET detectors

6) Susceptibility Artefacts

The homogeneity of Small variations in magnetic susceptibility leads to the entrance of PET system components into the magnet's bore to alter the magnetic field. Shimming RB may be used to precisely correct the gradient field's linearity, which is impacted by this. In order to ascertain the cause and extent of susceptibility artefacts, Stales et al. experimented using a small PET scanner prototype that uses T2-weighted imaging of the orange (McPET) and is compatible with magnetic resonance.

7) RF Interference

RF interference in PET-MRI arises because MRI requires highly sensitive receiver coils to detect NMR signals. Faraday shielding is essential to prevent non-uniform magnetic fields and eddy currents caused by high-frequency electronics. Improper shielding, such as asymmetric arrangements with Bruker Birdcage coils, negatively impacts MRI [24], while gamma shielding may further distort signals due to eddy currents.

B. Space and Time Constraints

Space and time constraints are also critical, MRI requires longer acquisition times (20–40 min) compared to CT (15 s–1 min), while modern PET with 3D, TOF, and extended FOV enables faster scans (3–15 min for brain, 10–20 min for whole body). In sequential designs, scan duration increases, whereas in simultaneous designs, overall time depends on the slower modality. Additionally, compact layouts are essential since sequential systems demand larger spaces for both standalone units [25].

V. PET IMAGE SEGMENTATION

Positron Emission as a functional imaging method, tomography assesses a radiotracer's three-dimensional bio-distribution within a specific organ or tissue. In several clinical and research studies, PET imaging has shown effective in the domains of neurology and cardiology, and cancer because of tracer properties. Since segmenting a PET image enables the transmission of tracer absorption inside a biologically significant area, it is an essential step in all PET applications. However, the labor-intensive, time-consuming, and highly variable nature of manual segmentation limited its use. As a result, several automated techniques for PET image segmentation were created. Cite the benefits, drawbacks, quality evaluation, and applications (Table VI) of the methodologies under study in order to choose the most appropriate approach for a certain circumstance.

A. Thresholding-based Image Segmentation

The most straightforward and widely used approach among those suggested for the difficult PET segmentation job is the threshold-based approach. One of these steps is to set a threshold value T to isolate the organ or lesion of interest from the background noise in a particular region of interest (ROI) or the entire image. Prior to threshold selection, these techniques typically transform the voxels into SUVs. When thresholding is used, all voxels larger than a threshold value are considered foreground, while all other voxels are considered background. To produce a binary image, this procedure is based on histogram analysis. Iterative, adaptive, and fixed thresholding techniques are the three primary categories into which thresholding techniques fall. For additional research, including tumor analysis and survival prediction based on texture indices, a number of thresholding techniques were employed because of their ease of use and great effectiveness.

- **Fixed Thresholding: The** foundation of fixed thresholding techniques is a fixed threshold, which can be chosen by a specialist, determined analytically using actual phantoms, or acquired via a training collection of images. To distinguish between benign and malignant tumors and to define gross tumor volume (GTV), a predetermined SUV threshold is often established at 2.5. Like all of the approaches listed below, GTV, often referred to as biological tumor volume (BTV), was established using the maximum standardised uptake value (SUVmax) at a certain site, expressed as a percentage. The conventional threshold for lesion segmentation, which is 40–43% of the SUVmax, has been the subject of several evaluations.
- **Adaptive Thresholding:** A number of adaptive thresholding techniques were put out in order to get around the drawbacks of fixed-threshold approaches. To determine the ideal threshold, generally speaking, Topt adaptive thresholding techniques consist of two phases. The first stage in the calibration process is to define mathematical formulas for the value of Topt based on early phantom research. These terms are then applied in healthcare environments to define hyperfixations on patient information. explain a few of these techniques to demonstrate some of the mathematical expressions that are employed.
- **Iterative Thresholding:** A priori knowledge of the lesion volume from structural imaging (like CT) or an analytical expression based on phantom geometry is necessary for adaptive thresholding methods, While iterative thresholding techniques do not require anatomical previous knowledge to estimate PET volumes, only the lesion's SBR, the reconstruction algorithm, the radiotracer, and these methods need the specific scanner's source-to-background threshold-volume curve. To choose the appropriate approach for a certain circumstance, evaluate the examined approaches and note their benefits, drawbacks, quality evaluation, and applications (Table VI).

10.48047/jocaaa.2024.32.01.72

B. Segmentation Based on Deformable Models in Cardiac Diagnosis.

In contrast to thresholding-based segmentation techniques, the non-rigid and mixed emotions of the heart have led to the widespread adoption of deformable models, which are sensitive to noise and complicated forms, for tracking cardiac images in ECG-gated and dynamic PET imaging. Cardiac PET image segmentation is in reality challenging due to the reality that breathing, cardiac contraction, and body posture all affect the location of the hear. Also, the resolution of cardiac imaging is generally lower than that of brain scans. The fundamental idea behind deformable models is to select an initial closed contour that iteratively minimizes a function to develop from its beginning position to a point of equilibrium. Parametric and geometric models are the two categories of deformable models. The basis of parametric models, also referred to as parametric active snakes or outlines, are parametric curves, surfaces, or volumes that undergo deformation due to either dynamic forces or energy functionals that include internal and external forces. An implicit function is represented by the level set method, is the foundation of geometric deformable models. Originally developed to address topological changes during curve evolution, depending on edge-based properties or regional intensity, this function deforms models.

- **Geometric Deformable Models:** Several research established deformable models based on level sets for PET segmentation. A multiphase level set approach was actually developed in [26] to employ both spatial and temporal data in order to partition 28 nonuniform frames of dynamic 18F-FDG PET imaging of mice into four dimensions. Next, a weighted absolute difference, rather than the more traditional least squares differences, was utilized in the data matching process to enhance the reliability of the estimations and rectify the inconsistent noise throughout the image frames. Additionally, a feature weighting approach that takes into account each frame's separation-to-noise ratio was employed to increase those organs' segmentation precision. The temporal activity curves (TACs) in manually chosen areas within the targeted organs serve as the basis for defining the weights. Each mouse image's kidney, heart, and bladder locations are used to manually initialize each level set function (LSF). This is equivalent to the zero level set of the function. The original image is then subjected to an affine transformation to align the locations of the previously determined targets.
- **Parametric Deformable Models:** Parametric models were introduced to address the challenges of geometric deformable models. It highlights the goal of segmentation based on the choice of radiotracer and presents some of the noteworthy works here. Myocardial perfusion has been estimated using 82Rb, 13N Ammonia, and 15O water tracers, whereas glucose metabolism has been estimated using 18F-FDG tracer. Using (DM-DSM), which stands for deformable models with a dual surface minimization technique, the heart volume was retrieved from the pulmonary anatomy and its position in the images of PET transmission. Markov Random Fields (MRFs) were employed to divide the transmitted image into four tissue classes: soft tissue (ST), lungs (LU), background (BG), and the region between the thorax and background. The surface extraction issue is redefined as an energy minimization problem subsequent to initialising DM-DSM with the MRFs segmentation outcome.

C. Mono- And Multi-Modal-Based Segmentation In Neurology Diagnosis

Neurology is very interested in PET imaging since it offers a strong tool for studying the aetiology and development of neurological diseases like Parkinson's and Alzheimer's based on the radiolabeled molecules employed. It was frequently necessary to understand the plasma time-activity curve is another name for the cerebral input function (IF), in order to quantify brain PET data and estimate the cerebral metabolic rate of glucose (CMRglc). Invasive and time-consuming arterial blood sample is the traditional method used to determine IF. As a result, image-derived input functions are a non-invasive substitute for arterial sampling; however, they frequently necessitate the identification of ROI. It was possible to automatically delineate ROIs on PET scans directly or indirectly by using additional anatomical modalities to co-register PET scans.

- **Mono-Modal Brain PET Image Segmentation:** To autonomously separate ROIs in cerebral PET data, many methods have been proposed. For instance, k-means, which is based on two hierarchical stages, and In order to estimate the cerebral vasculature TAC derived from the PET dataset that contains [18F]-altanserin. The data can be divided into a few rough clusters in the first step. To better recover the vascular ROI, these clusters were taken out and subjected to the clustering method in the second step. A 3D visual evaluation of the homogeneity of the identified clusters and a within-variance measure, which employed significant fluctuations in the number of clusters k, was established at this stage utilizing within-class inertia. The quantity of clusters k ranged from 1 to 10. There is substantial agreement (t P <0.05) between the distribution volume (DV) values obtained from the k-means-clustered time-activity curves (TACs) and the arterial and venous blood samples.
- **Segmentation of Multi-Modal Brain PET Images :** A popular strategy for overcoming Indirect ROI identification is made possible by the coregistration of PET scans to many anatomical modalities, which is a shortcoming of region-based analysis of PET data and algorithms for segmenting monomodal brain PET images. In actuality, image segmentation is improved when two modalities are used because of the greater enhanced clarity and reduced noise in CT or MRI data, such PET/CT and PET/MRI, which are combined. Furthermore, in the early phases of a disease process, PET can identify minute functional alterations. CT and MRI, on the other hand, offer comprehensive anatomical data. Therefore, multi-modal PET image segmentation techniques (PET/CT or more recently, PET/MRI) have drawn increased interest in recent years because of the frequent necessity for precise illness type diagnosis and characterization. To automatically identify brain

10.48047/jocaaa.2024.32.01.72

ROIs, for example, an automated technique was created that uses the conversion and registration of magnetic resonance data based on atlases. After that, TACs were created, and the PET radioligand binding's regional binding potential (BP) was measured. The actual procedure starts with matching a set of predetermined ROIs in a conventional brain template to individual high-resolution MR images. Refinement is the next step, which entails eliminating extra voxels and adding nearby missing voxels to the ROIs. This stage is based on the likelihood that each voxel is part of the grey matter, which is created using the statistical parametric mapping (SPM2) segmentation method and a Gaussian-smoothing filter. Then, using The individual refined ROIs are converted to the PET image space using the normalized mutual information (NMI) approach, which involves co-registering the individual MR images with the PET images.

TABLE VI. COMPARISON OF MEDICAL PET IMAGE SEGMENTATION METHODS[27]

Method		Principle	Applications	Advantages	Limitations
Thresholding methods	Fixed	Uses a pre-defined SUV value (e.g., SUV = 2.5 or % of SUVmax) to segment lesions.	Oncology (tumor volume delineation, malignant vs benign lesion differentiation).	Simple, fast, widely used in clinical practice.	Not adaptable to different tumor sizes, shapes, or noise; ignores heterogeneity.
	Adaptive	Optimal threshold (Topt) derived from phantom studies and mathematical expressions.	Tumor delineation with more accuracy than fixed threshold.	Accounts for lesion contrast and background; better generalization.	Requires phantom calibration; depends on scanner and tracer.
	Iterative	Iteratively refines threshold using lesion-to-background ratio and scanner response curves.	Oncology and survival prediction studies.	Does not require anatomical priors; more accurate for irregular shapes.	Computationally more complex; dependent on scanner-specific parameters.
Deformable models	Geometric	Evolves contour using implicit functions and regional intensity/edge features.	Cardiology (ECG-gated and dynamic cardiac PET), Neurology.	Handles topological changes; robust for noisy/blurry PET.	Initialization sensitive; computationally intensive.
	Parametric	Parametric curves/surfaces evolve based on energy minimization with internal/external forces.	Cardiac segmentation (heart, lungs, thorax), tracer-specific studies.	Good for organ boundary extraction; incorporates anatomical priors.	Sensitive to initialization; can get trapped in local minima.
Mono- and multi-modal-based segmentation methods	Mono-Modal	Techniques like k-means and TACs for direct clustering or region-of-interest extraction from PET scans.	Neurology (return on investment for vascular TAC, Alzheimer's disease, and Parkinson's disease).	PET-based; non-invasive; does not need collection of arterial blood.	Less accurate for tiny ROIs; lower resolution; sensitive to noise.
	Multi-Modal	PET/high-resolution CT/MRI co-registration; atlas-based ROI enhancement.	Specialities in neurology and oncology (disease categorisation and diagnosis).	Improves ROI accuracy by combining functional (PET) and anatomical (CT/MRI) data.	Possible registration mistakes; another imaging modalities needed.

VI. PET DETECTOR MODULE

There is a significant agreement (t P <0.05) between the distribution volume (DV) values obtained from the k-means-clustered TACs and the arterial and venous blood samples.. The inorganic scintillator reacts rapidly and momentarily, producing light photons from deposited γ-energy. A photodetector converts the scintillator's light pulse into analogue or digital data through optical connection. Numerous configurations are possible for a scintillator-based PET detector module. For example, the traditional γ-camera technique is shown in Figure 11a, where many photodetectors are coupled to a wide area continuous or monolithic scintillator [28]. To optimize the light collection of the photodetectors, a reflecting coating is applied to the scintillator. The coordinates of the point of interest (POI) are determined by using the light that reaches the photodetectors, which is deliberately enlarged by the process of creating a refractive index mismatch using a light guide. The partial energy that each photodetector collects separately is added to determine the energy of the absorbed γ-photon. This method's primary drawback is that it disables a huge detector region during a certain dead period when a γ-photon detection takes place, which severely limits the highest possible single count rate.

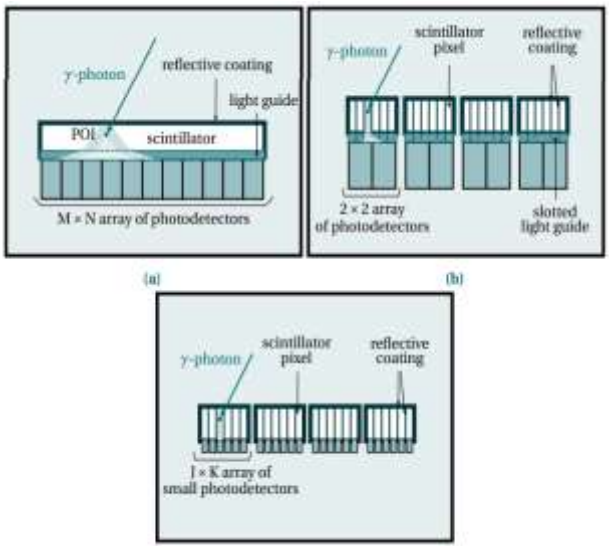

Fig. 11. Examples of popular PET module setups. (a) type of detector based on a gamma camera. (b) Type of BGO block detector. (c) kind of one-to-one coupling detector.

A more effective technique is to connect a 2 × 2 array of photodetectors to an array of pixelated scintillators using a

10.48047/jocaaa.2024.32.01.72

slotted light path, where each pixel is coated in a reflecting material (see Figure 11b). This concept uses a slotted light guide to manage the light sharing between photodetectors in order to encode scintillator pixels. Compared to the γ-camera technique, this method produces a greater single count rate at the same radioactive dosage and enables the modular construction of vast detection regions.

PET detector modules, which further divide the detection region, are developed by optically linking tiny photodetectors and scintillator pixels one-to-one (see Figure 11c). For this method to read out the output signals from the photodetectors, a greater degree of integration and complexity are needed [29]. For high spatial-resolution PET, such as tiny animal PET imaging, pixellated scintillators need an extremely small pixel pitch. The ratio of the regions of the γ-sensitive detector to the total detector areas, known as the packing percentage, may be significantly reduced by the amount of space between the photodetectors and the reflective coating's thickness. The reflective coatings are made using thing reflective sheets to get a good packing fraction [30]. Furthermore, the detector performance is impacted by inter-crystal Compton scattering between scintillator pixels in small-pitch scintillator pixels. Miniaturized variants of the γ-camera technique were used in alternative designs to successfully get a high spatial resolution while maintaining a satisfactory packing fraction. Furthermore, nonlinear estimate techniques based on the light spreading of the POI are used to derive the DOI information. Additionally, estimating the DOI of the POI using double-sided readout has been proposed; however, this method requires twice the number of photodetectors needed [31].

A. Scintillating Inorganic Crystals-Based Detectors

Sodium iodide (NaI(Tl)) with lutetium-yttrium oxy orthosilicate (LYSO), bismuth germanate (BGO), and lanthanum bromide (LaBr3:Ce), and several more substances are examples of common materials. Their excellent detection efficiency, capable of counting at a pace of up to 107 counts per second, remarkable energy resolution, and time resolution, and, lastly, their variety in size and construction all contribute to their considerable significance. The primary qualities needed for a sparkling crystal are as follows:

- A high atomic number of the primary ingredient and a high material density between 3 and 7 g/cm^3 enable excellent gamma ray detection efficiency (high "stopping power").
- The fluorescent component of the crystal decays slowly, producing quick signals that enable high counting rates.
- Enhanced photon statistics and, thus, ER due to a high light yield.
- Minimal response nonlinearity that results in a little energy decrease.
- Radiation hardness and chemical stability.
- The photodetector peak response and they match the wavelength of the crystal peak emission.

Thallium-activated alkali halide crystals, like NaI, NaCl, and NaBr, were the first scintillating crystals used to find gamma rays. The emission extends to the visible range if the thallium concentration is high (0.1 to 5 molar percent); If it is very little, less than 0.1 molar percent, it emit light in the ultraviolet (UV) spectrum. NaI(Tl) is an example of a nonconducting crystal. This indicates that its empty conduction band and full valence band have a significant energy difference. The kinetic energy of energetic electrons is reduced when they form electron-hole pairs through gamma interactions with NaI materials. These couples can recombine to release energy as lattice vibrations or emit light through radiative transitions. The addition of thallium at a 10^{-3} molar proportion acts as an activator, greatly increasing the crystal's light emission. Luminescence happens in a matter of microseconds due to the exponential decay rule and huge decay constant of thallium's radiative emission. This makes it possible to distinguish between various scintillation events throughout time, which is essential for determining when gamma photon energy depositions occur.

VII. Literature Review

Recent studies on PET detector modules focus on improving spatial, energy, and timing resolutions through advanced scintillator designs, surface treatments, and readout techniques. Here review the recent studies of PET Detector Modules using crystal technology as shown as below in Table VII.

Peng et al. (2023) built a detector module for energy, space, and time that uses a slab of LYSO crystal that is 40 x 40 x 3.72 mm3 in size. The crystal's six sides were polished, and the top and bottom sides were covered with enhanced specular reflector (ESR). Four arrays of 8x1 Broadcom AFBR-S4N44C013 SiPMs were connected to the other four sides. After detecting the scintillation light, the SiPMs received 32 analogue signals, each of which was digitalized using PETsys' TOFPET-2 FEM128 system. The pattern of scintillation light on the 32 SiPMs and the gamma ray contact point, which are intimately connected, were interpreted using a convolutional neural network (CNN). Overall, the detector has an ER of 11.9% after SiPM saturation correction, a temporal resolution of 563.6 ps FWHM, and a 1.56/1.53 mm FWHM spatial resolution in both the x and y axes [32].

Liu et al. (2023) suggested method maximizes multichannel and multifunctionality by utilizing the FPGA's voltage-referenced standard instead of the LVDS standard. The LVDS receiver and the voltage-referenced receivers were evaluated for linearity discrepancies. Based on the suggested topology, the construction of a PET detector module necessitated the development of a 32-channel electronics prototype for the purpose of testing the intended use in radiation detector applications. The detector has two silicon photomultipliers (SiPM) at either end that are directly connected to a 15 × 15 LYSO array. In the middle, the mean ER for a single crystal might reach 17.9%. One approach to managing a small, multichannel electronics readout system is the voltage-referenced receiver-based linear discharge technique [33].

Kim et al. (2022) develop a prototype system with four detector modules housed in a 115 mm outer-diameter cylindrical supporting frame. Eight units, each consisting of a 4x4 Hamamatsu MPPC array (14161-3050HS-04) is coupled to a 12x12 array of 1x1x10 mm3 LYSO crystals, make up each detector module. Six outputs are produced for the full detector module using a highly multiplexed readout that uses resistor networks and straplines constructed on an 185 mm x 30 mm printed circuit board. CAEN DT5742 digitisers are used to capture and process the output signals offline. It discusses the possibility of a complete detection system and

10.48047/jocaaa.2024.32.01.72

presents the initial findings from the proto-type PET system [34].

Yu et al. (2022) the qualities and examination of the scintillation crystal specs used by several PET scanners, along with the introduction of the scintillation crystal principle. The scintillation crystal with the best overall characteristics at the moment is Lu2(1−x)Y2xSiO5 (LYSO). LaBr3's deliquescence has prevented it from being used in any PET scanner, even though it offers even better timing characteristics and light output. High DOI resolution and significant application possibilities are demonstrated by Gd3(Ga, Al)5O12 (GAGG) detectors. PET's future expansion aims to achieve great sensitivity and high spatial resolution, which calls for scintillation crystals with improved performance. PET's application sectors are also continuously growing [35].

Lee and Baek (2021) in order to generate the look-up table, a DETECT2000 simulation was run using a 6 x 6 scintillation pixel array with a 4 × 4 array of SiPM photo sensors. Using the Anger equation, the light signals from the gamma interaction at the middle of each scintillation pixel were cut down to four channels. The ratios of each channel were then used to create the LUT. Utilizing this experiment-derived data, it demonstrated a 90% accuracy rate. Even though the simulation produced the LUT, this technique may be used with a traditional detector module as MLPE uses the ratio of each channel to estimate the scintillation pixel's position. By altering a traditional methodology, this novel technique allows the scintillation pixel's location to be converted into digital coordinates without the need for further procedures [36].

Zeng et al. (2021) provide an assessment of a demonstration system that is fully functional to allow for the reporting of increased detector module performance. Six detector modules comprise the 12-sided ring-shaped device with an axial length of 25 mm and a diameter of 108 mm. Its findings reveal an 18.9% ER and a 354 ps coincidence timing resolution at 511 keV. The energy window of the scanner is 450-650 keV, and its basic sensitivity is 1.11%. The three distinct spatial resolutions in axial, radial, and tangential axes are 2.08, 2.19, and 2.24 mm, correspondingly. Employ a recovery strategy for the same data since inter-crystal scatter (ICS) has the potential to lead to a loss of system count. Consequently, In the uniform zone, an image quality phantom's sensitivity rises by 83% and its signal-to-noise ratio rises by 19%. However, note a loss of 7–12% in spatial resolution and a degraded temporal resolution of 419 ps [37].

Wu, Lee and Levin (2020) GATE simulated a module that use 3x3x3 mm3 effective detector voxels and a 3D position-sensitive scintillation detector with long crystals that uses SiPMs to read out from the side. The results showed that NN ICS event placement accuracies were from 0.753 to 0.680 when the number of contacts per annihilation photon was between 2 and 5. For the same range, the accuracies for LTA were between 0.726 and 0.367, and for WTA they were between 0.613 and 0.251. Then, in order to evaluate image quality, contrast and resolution phantoms are recreated using the PET brain imaging system with a 25 cm diameter using the single-detector simulation. WTA and LTA were 0.046, 0.178, and 0.034, 0.140, respectively, whereas the NN model's image-normalized. The mean absolute errors for the resolution and contrast phantoms were 0.122 and 0.030, respectively. The NN demonstrated improvements in Contrast Recovery (from resolution phantom) of 6.04 to 8.95%, Modulation Transfer Function values ranging from 2.13 to 6.34% and Contrast Noise Ratio values ranging from 0.53 to 2.85% as compared to the second-best LTA. For these NN relative improvements, the top bound was obtained using features at the virtual system's upper bound on spatial resolution (2 mm). Most quantification figures of merit and image quality are improved by the NN positioning approach that is being studied, according to the results [38].

Deng, Deng and Chen (2020) A LIGHTENING® PET detector was made by using a 13 × 13 lutetium-yttrium oxyorthosilicate (LYSO) crystal array and a 6 × 6 silicon photomultiplier (SiPM) array. Thus, a new sampling technique called the dual time interval (DTI) approach is suggested to achieve digital rapid scintillation pulse capture. The resolution of the crystal array's edge area is significantly increased by the construction of a semi-cut light guide. It is evident from the produced flood histogram that all 13 × 13 crystal pixels may be distinguished from one another. The quality of the flood histogram was evaluated under several test scenarios, the detector's ideal working conditions were determined. The results showed that the average energy resolution was 14.3% and the coincidence timing resolution was 972 ps. The experimental results suggest that the LIGHTENING® PET detector could be used to make a better time-of-flight PET scanner because it has such a high resolution[39].

A. Research Gap Analysis

Despite significant advances in PET detector module development, several gaps remain. As summarized in Table VII, recent designs have explored approaches such as optimized surface treatments and reflector configurations, wavelength-shifting fibre readouts, depth-of-interaction (DOI) algorithms, large-crystal CNN decoding, light-guided readouts, and system-level demonstrators. While these innovations have improved individual metrics such as CTR, energy resolution, and spatial/DOI resolution, limitations persist—CTR values in many detectors remain above 500 ps, DOI performance is often validated only in simulations, and challenges with calibration complexity, scalability, and computational overhead hinder practical integration. Additionally, although alternative scintillator materials with superior timing or DOI potential exist, most systems still rely on LYSO due to stability, leaving performance gains untapped. The research gap, therefore, lies in developing a unified detector architecture capable of achieving CTR below 300 ps, ER under 10%, and DOI resolution under 3 mm, while maintaining scalability and cost efficiency for clinical and brainPET systems.

TABLE VII. SUMMARY OF PET DETECTOR MODULE STUDIES USING SCINTILLATION CRYSTALS TECHNOLOGY

Author	Detector / Method	Crystal Specs	Experiment	Key Performance	Limitations
Peng et al., 2023	Large LYSO slab + CNN decoding of Sip signals	LYSO 40×40×3.72 mm³, polished, ESR-covered	Experimental + CNN	11.9% energy, 1.56 mm spatial, 563.6 ps CTR	CTR higher (worse) than state-of-art; CNN adds computational overhead; scaling to large systems uncertain

10.48047/jocaaa.2024.32.01.72

Kim et al., 2022	Prototype PET system with four cylindrical detector modules; highly multiplexed readout using resistor networks and striplines	12×12 array of 1×1×10 mm³ LYSO crystals per unit; 4×4 Hamamatsu MPPC array per unit	Preliminary results obtained from prototype; off-line signal processing with CAEN DT5742 digitizers	Demonstrated feasibility of prototype system and potential scalability	Only preliminary results; full system performance yet to be validated
Liu et al., 2023	32-channel FPGA-based electronics readout using voltage-referenced standard; PET detector module	15×15 LYSO array; dual-ended Sip readout	Validation of voltage-referenced readout; energy resolution measurement	Mean energy resolution of 17.9% at center; compact and multichannel readout demonstrated	Limited to prototype; performance across full module or large-scale system not tested
Yu et al., 2022	Review of scintillation crystals (LYSO, $LaBr_3$, GAGG)	Various	Review study	LYSO = balanced; $LaBr_3$ = best timing but hygroscopic; GAGG = good DOI	No new module design; lacks experimental validation of alternatives
Lee & Baek, 2021	LUT-based positioning with DETECT2000 + Anger logic	6×6 scintillator + 4×4 Sip	Simulation + experiment	90% positioning accuracy	Accuracy depends on calibration quality; may degrade in larger/more complex modules
Zeng et al., 2021	12-sided PET ring system (Ø108 mm, 25 mm axial)	6 detector modules	Experimental demonstrator	18.9% energy, 354 ps CTR, sensitivity 1.11%	Slight loss in CTR (419 ps) & spatial resolution (7–12%) after ICS recovery
Wu, Lee & Levin, 2020	3D scintillator module with Sip side-readout + NN	3×3×3 mm³ voxels	GATE MC + NN	NN: higher accuracy & 6–9% better contrast recovery	Needs high computational resources; limited experimental proof
Deng, Deng & Chen, 2020	LIGHTENING® PET detector with semi-cut light guide + DTI sampling	13×13 LYSO + 6×6 Sip	Experimental	14.3% energy, 972 ps CTR, clear pixel separation	CTR relatively poor (>900 ps); may limit TOF-PET applications

VIII. Method and Material

This study employed a combined experimental and Monte Carlo (GATE/GEANT4) simulation approach to evaluate PET detector modules using various scintillator materials (LYSO, LSO, GAGG, BGO, $BaSO_4$) in multiple geometries (cuboid, pixelated, monolithic, dual-layer). Crystals were coupled to SiPMs with fast ASIC/FPGA-based electronics to record 511 keV photon events. CTR was derived from coincidence histograms, ER from Gaussian fits of the photopeak, and Depth-of-Interaction (DOI) from dual-ended or monolithic readouts. Simulated results incorporating scintillation yield, decay time, and surface treatments were validated against prototype measurements to optimize detector design for high-performance PET imaging.

A. Scintillator Configurations and Parameters

This study investigates a diverse set of scintillator configurations to evaluate their impact on PET detector performance, focusing on CTR, ER, and Depth-of-Interaction (DOI) resolution. The crystals used include LYSO, GAGG, BGO, $BaSO_4$, and LSO, each selected for its unique scintillation properties, decay time, and relevance to clinical imaging. Configurations span various geometries—monolithic blocks, pixelated arrays, elongated bars, and dual-layer stacks to assess how crystal shape and size influence detection precision. The simulation and design parameters form the backbone of this study's performance evaluation framework for PET detector modules. The following physical and architectural characteristics of the detector modules are illustrate in Table VIII.

TABLE VIII. Design Parameters for PET Detector Module Configurations

Parameter	Value / Description
Crystal Material	LYSO, GAGG, BGO, $BaSO_4$, LSO
Crystal Dimensions	Ranges from 0.95×0.95×20 mm³ to 50×50×15 mm³
Pixel Pitch	1.6 mm, 3.2 mm (for arrays)
Layering	Single-layer and dual-layer configurations
Array Format	8×8 pixelated arrays, monolithic blocks
Sip Size	Typically matched to crystal cross-section (e.g., 3×3 mm²)
Readout Electronics	Fast amplifiers, TDCs, ADCs, and FPGA-based logic
Coincidence Setup	Reference detector paired for CTR measurement
Mechanical Alignment	Precision holders to ensure reproducible geometry

In simulation, photon energy was fixed at 511 keV to replicate positron annihilation events. Material-specific scintillation yields and decay times were modeled to reflect realistic light output and timing behavior—LYSO offering high photon yield and fast decay, while BGO and GAGG provided contrasting profiles. Surface treatments (polished vs. unpolished) and refractive indices were incorporated to simulate light transport dynamics, with Monte Carlo-based photon tracking (e.g., GEANT4 or GATE) used to model optical paths and interactions.

B. Data Acquisition and Processing

The data acquisition (DAQ) system is responsible for capturing, digitizing, and processing signals from the PET detector modules. It ensures accurate timing and energy measurements essential for image reconstruction and performance evaluation. Key Components and Workflow:

- **Signal Capture:** Analog signals from SiPMs are collected upon gamma photon interaction with the scintillator.
- **Digitization:** Signals are digitized using high-speed electronics—typically custom ASICs (e.g., TOFPET2, STiC) or FPGA-based systems—with sampling rates up to 1 GS/s.
- **Timestamp Extraction:** Timing information is derived using modern methods for accurate coincidence timing resolution (CTR), such as constant fraction or discriminating.
- **Energy Calibration:** Pulse height analysis is performed to determine energy resolution, often using Gaussian fits to the 511 keV photopeak.

10.48047/jocaaa.2024.32.01.72

- **Temperature Compensation:** Gain variations due to thermal drift are corrected using onboard calibration routines.
- **Data Handling:** Digitized data are streamed to a host PC or embedded processor for real-time or offline analysis, including DOI decoding and event filtering.

C. Simulation and Modeling

Simulation and modeling were employed to validate the experimental performance of PET detector modules and to optimize design parameters before fabrication. Monte Carlo methods, notably using GATE (Geant4 Application for Tomographic Emission), were used to copy how photons interact, how detectors are set up, and how electronics respond.

1) Simulation Objectives

- **Performance Prediction:** Estimate CTR, Energy Resolution, and DOI accuracy.
- **Design Optimization:** Evaluate the impact of crystal size, SiPM layout, and readout electronics on spatial and timing performance.
- **Validation:** Compare simulated results with experimental data to confirm the fidelity of the physical system.

2) Geometry and Material Modeling

- **Crystal Arrays:** Pixelated and monolithic LYSO crystals were modeled with precise dimensions (e.g., 4×4×20 mm³, 32×32×20 mm³).
- **Photodetectors:** SiPM arrays (analog and digital) were positioned to match experimental coupling schemes, including dual-ended readout for DOI encoding.
- **Reflectors and Optical Interfaces:** Light guides, Teflon wrapping, and optical grease layers were included to simulate realistic photon transport.

3) Photon Interaction and Transport

- **511 keV gamma photons:** simulated from situations where positrons and electrons collide, tracking Compton scattering, photoelectric absorption, and escape probabilities.
- **Scintillation Light Generation:** Modeled based on LYSO properties—light yield, decay time, and emission spectrum.
- **Optical Photon Tracking:** Simulated light propagation through the crystal, including reflections, refractions, and absorption at interfaces.

4) Electronic Response Modeling

- **SiPM Behavior:** Gain, dark count rate, and timing jitter were incorporated to reflect realistic signal generation.
- **Signal Processing:** Electronic models included shaping, thresholding, and digitization using ASICs (e.g., TOFPET2, STiC) or FPGA logic.
- **Timing Algorithms:** Constant fraction discrimination and leading-edge techniques were simulated to extract timestamps.

5) DOI Estimation

In modules employing dual-ended SiPM readout or monolithic scintillator crystals, to measure the depth of interaction (DOI), the distribution and attenuation of scintillation light within the crystal volume were modelled. These simulations modeled how optical photons propagate and are shared between opposing SiPM arrays or across the monolithic surface, allowing the reconstruction of the interaction depth based on relative signal intensities. DOI resolution was quantified by comparing the reconstructed depth values with the true interaction positions, typically determined using collimated beam experiments or tagged sources.

6) Validation and Comparison

To validate the simulation framework, key performance metrics including Coincidence Timing Resolution (CTR), energy spectra, and DOI profiles were compared against experimental measurements from physical detector prototypes. Discrepancies between simulated and measured results were analyzed to refine the models, such as adjusting SiPM gain maps, modifying crystal surface reflectivity, and incorporating temperature-dependent behavior. These refinements ensured that the simulation outputs closely matched real-world performance, enhancing the reliability of predictive modeling for future PET module designs.

D. Crystal Scintillator Technologies

The study incorporates a range of scintillator technologies, each selected for its distinct physical and optical properties that influence PET detector performance.

1) LYSO (Lutetium-Yttrium Oxyorthosilicate) and LSO (Lutetium Oxyorthosilicate)

LYSO is one of the scintillation crystals that are most often utilized in contemporary PET systems. Its high density (approximately 7.1 g/cm³) and high effective atomic number make it very good at blocking 511 keV photons. It has a short decay time of 40 ns and an estimated light output of 32,000 photons/MeV. This makes it great for timing resolution and especially good for time-of-flight (TOF) PET applications. Moreover, it provides good ER (~10%). However, due to the presence of Lutetium, the material is expensive, which is a practical limitation. Despite this, LYSO remains the recommended option for the majority of cutting-edge clinical PET scanners.

2) GAGG (Gadolinium Aluminum Gallium Garnet)

GAGG: There is ongoing research into ce, a more recent scintillator. The light production is quite large, frequently exceeding 40,000 to 50,000 photons/MeV in several configurations, relatively good energy resolution, and the advantage of no intrinsic radioactivity, which is helpful for low-count or single-photon work [40]. The decay time is slower than LYSO, which may reduce time resolution in TOF-PET, but for many applications, its strengths make it attractive

3) BGO (Bismuth Germanate)

BGO was one of PET scanners were among the first to employ scintillation crystals, particularly in the 1980s and 1990s. Excellent photon absorption efficiency is provided by its high atomic number and extremely high density of 7.1 g/cm³. This property allows BGO to achieve high sensitivity in PET imaging. Having a length of around 300 nanoseconds, its decay time is lengthy, and its light production is quite modest at around 8,000 photons/MeV. These characteristics result in poor timing resolution and make it unsuitable for TOF PET. Additionally, the ER of BGO is worse than modern alternatives (~15–20%). Despite these drawbacks, BGO

10.48047/jocaaa.2024.32.01.72

played a significant role in early PET systems due to its strong photon detection capability.

4) $BaSO_4$ (Barium Sulfate)

$BaSO_4$ is not a scintillator but is widely used as a reflective coating in PET detector modules. It has high reflectivity and excellent chemical stability, which makes it effective in enhancing the light collection efficiency of scintillation crystals. By reflecting stray photons back into the photodetector, $BaSO_4$ increases the quantity of light that may be used and enhances the overall performance of the detector. It is also inexpensive and easy to apply, which has led to its common use in detector designs. However, since it does not produce scintillation light itself, its role is limited to being a supporting material rather than a primary detector crystal.

E. Measuring Parameters

To assess the performance of PET detector modules, several quantitative parameters are measured. These include CTR, ER, and DOI resolution. Each metric reflects a critical aspect of detector functionality and is derived using standard analytical methods.

1) Timing Resolution of Coincidence

CTR is an important number for TOF-PET systems, representing the temporal precision between two coincident gamma photon detections. A popular method for representing the time difference histogram between two detector modules is to use its FWHM. It may be calculated mathematically using the timing distribution's standard deviation: Equations (1) through (3) were used to determine the temporal difference (Δt) of two photons that are destroyed in a positron decay [41][42]:

$$\Delta t = t_A - t_B \quad (1)$$

$$t_A = (t_1 - t_2)/2 \quad (2)$$

$$t_B = (t_3 - t_4)/2 \quad (3)$$

The time stamps representing the threshold crossing from the two detectors' four Sip arrays coincidentally were denoted as (i = 1…4), and the timing information for detectors A and B were denoted as t_A and t_B , respectively.

2) Energy Resolution (ER)

The energy resolution of the detector, especially the 511 keV photopeak from positron annihilation, is used to quantify its ability to discriminate between various gamma photon energies. It is computed using Equation (4) ratio of the photopeak's FWHM to centroid:

$$ER\% = \frac{FWHM}{Centroid} \times 100 \quad (4)$$

High energy resolution (typically 10–15% for LYSO crystals) ensures effective rejection of scattered photons and enhances image fidelity.

3) Depth-of-Interaction (DOI) Resolution

DOI resolution is essential for minimizing parallax error in PET systems, especially those with thick crystals or wide ring geometries. For modules with dual-ended SiPM readout or monolithic crystals, DOI is estimated by analyzing the relative signal intensities across the detector surface or between opposing SiPM arrays. The accuracy of DOI estimation is expressed as Equation (5):

$$DOI_{error} = |Z_{reconstructed} - z_{true}| \quad (5)$$

Where $Z_{reconstructed}$ is the estimated depth and z_{true} is the actual interaction location. DOI resolution is typically reported in millimeters, with values around 2–4 mm FWHM considered effective.

Together, these parameters provide a comprehensive framework for evaluating and comparing PET detector modules across different design architectures and application contexts.

IX. Comprehensive Results Analysis

This section evaluates various PET detector crystal configurations based on two key performance metrics: CTR, and ER as shows in Table IX. It includes tabular comparisons, visual plots, and spatial maps to assess detector precision and uniformity. This analysis highlights the trade-offs between crystal geometry, material, and readout configuration. GAGG offers superior energy resolution, while LYSO excels in timing precision. Dual-layer designs improve CTR but add complexity. DOI performance varies significantly across materials, with polished BGO underperforming.

TABLE IX. Crystal configurations based on CTR and energy resolution

Configuration	CTR (ps)	Energy Resolution (%)
LYSO 2.98×20 mm[43]	180	10.2
LYSO 1.95×30 mm[43]	263	11.7
BGO Polished[44]	3200	16.9
BGO Unpolished[44]	3500	17.7

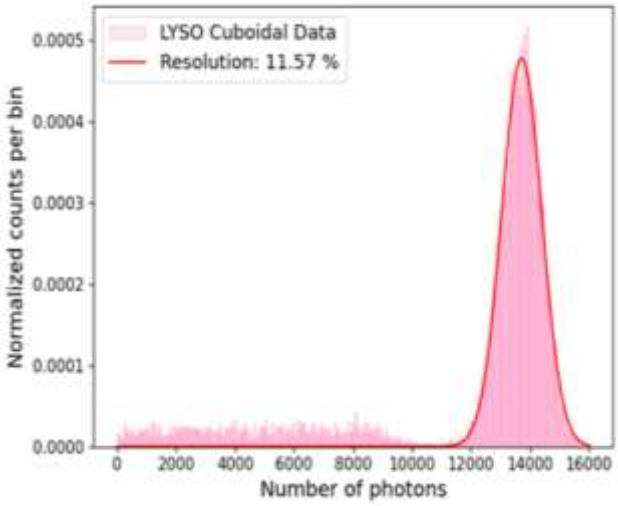

Fig. 12. Energy resolution plots for LYSO Cuboid

Figure 12 shows the LYSO Cuboid detector's energy resolution curve. Histogram (in pink) showing normalised count distribution with respect to photon count. To estimate the energy resolution, a solid red curve representing a Gaussian fit is superimposed on top of the histogram. The detector's average response to a certain energy input is shown by the peak that emerges close to 13,000 photons. With a computed energy resolution of 11.57%, the detector's capacity to discriminate between various energies is demonstrated; a smaller percentage denotes superior resolution.

10.48047/jocaaa.2024.32.01.72

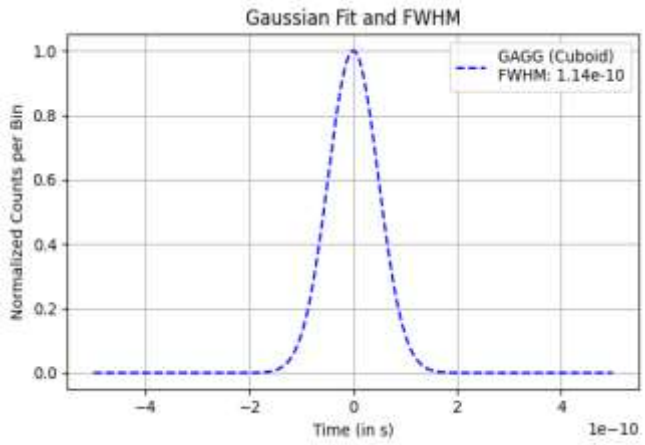

Fig. 13. CTR values for various geometries of GAGG crystals

Figure 13 illustrates a Gaussian fit (shown as a dashed blue line) applied to a distribution of events, likely representing a temporal or pulse shape measurement. The x-axis displays time in seconds, while the y-axis shows the number of counts per bin that have been normalised. The data is centered around $t = 0$ t=0 and displays a sharp, symmetric peak typical of a Gaussian distribution. According to the legend, the material analyzed is GAGG (Cuboid), and the fitted Gaussian's Full Width at Half Maximum (FWHM) is $1.14 \times 10 - 10$ 1.14×10 −10 seconds (114 picoseconds), indicating the temporal resolution or spread of the distribution. The time axis spans approximately $- 5 \times 10 - 10$ −5×10 −10 s to $+ 5 \times 10 - 10$ +5×10 −10 s, and the normalized counts reach a maximum value of 1.0. A grid is included in the plot to aid visualization of the data points.

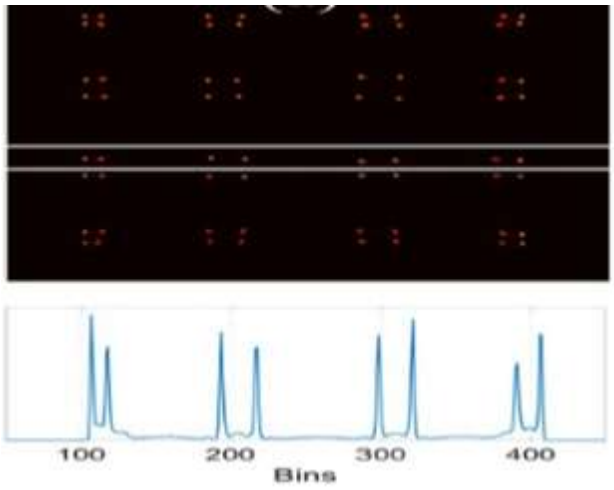

Fig. 14. Flood histograms for LYSO 2.98×20 mm

The flood histogram analysis for a LYSO crystal of dimensions 2.98×20 mm in Figure 14, showcasing spatial event localization and signal uniformity. The top section displays a grid of bright orange clusters on a black background, representing detected scintillation events across the crystal surface. These clusters are symmetrically distributed, indicating consistent light output and effective pixel separation. The bottom section features a line graph of normalized counts versus bin number, with sharp, periodic peaks corresponding to the spatial clusters above. This dual representation confirms the crystal's ability to resolve discrete interaction positions, validating its suitability for high-resolution imaging applications.

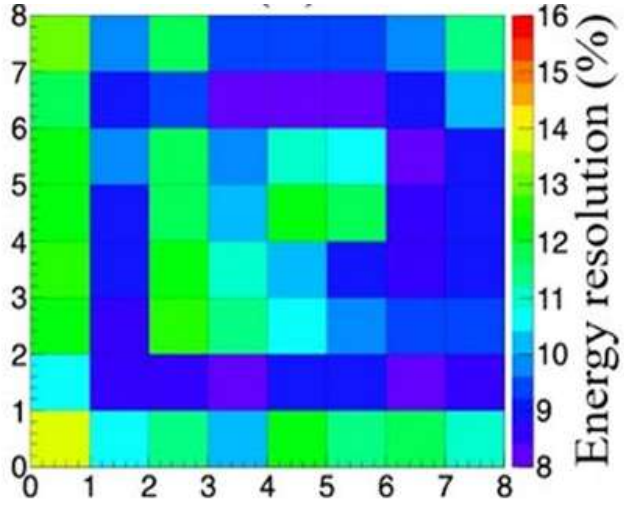

Fig. 15. Energy resolution map for LYSO 2.98×20 mm

Figure 15 shows the ER map for this LYSO crystal is 2.98 x 20 mm. The color-coded scale ranges from 8% to 16%, where lower values (blue shades) indicate better ER and higher values (green to red) represent poorer resolution. The map reveals a spatial variation across the crystal, with the central region showing moderately higher resolution (around 11–13%) compared to the outer regions, where both lower (≈8–10%) and higher (≈14–16%) values are observed. This distribution highlights the non-uniform energy response of the crystal, which is critical for performance evaluation in detector applications.

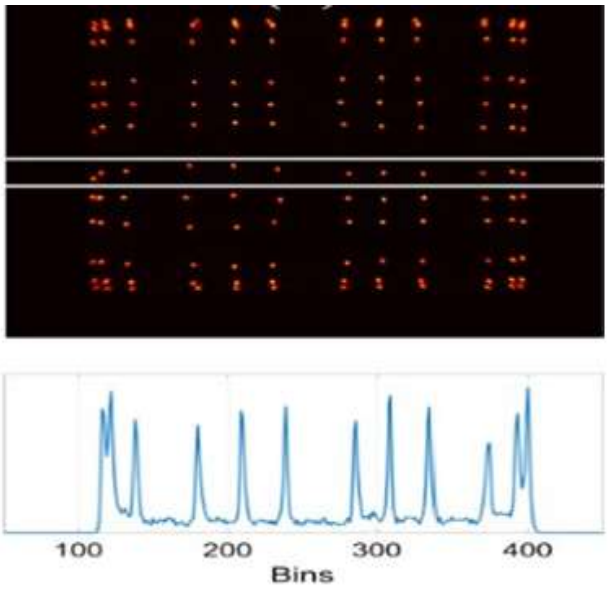

Fig. 16. Flood histograms for LYSO 1.95×30 mm

The flood histograms obtained from the LYSO crystal with dimensions of 1.95 × 30 mm are shown in Figure 16. The top image displays a well-defined array of bright spots corresponding to individual crystal pixels, demonstrating good crystal separation and uniformity in light distribution. The lower plot illustrates the bin profile, where distinct peaks appear at regular intervals, further confirming clear pixel identification. The uniform separation of peaks indicates

10.48047/jocaaa.2024.32.01.72

efficient crystal discrimination and highlights the crystal's suitability for precise position-sensitive detection in PET or related imaging systems.

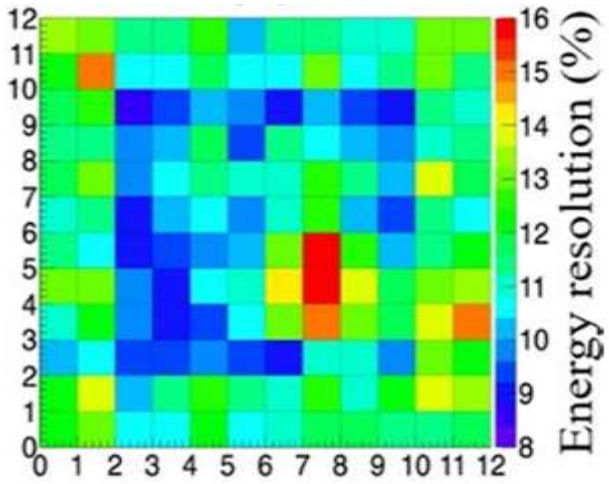

Fig. 17. Energy resolution map for LYSO 21.95×30 mm

Figure 17 shows the spatial ER map for a LYSO crystal that is 21.95×30 mm, highlighting performance variations across its surface. The heatmap uses a color gradient ranging from dark blue (8%) to red (16%) to represent ER percentages, with the x-axis spanning 0 to 12 and the y-axis from 0 to 10. A concentrated red region near coordinates (7, 5) indicates the highest ER value, suggesting localized degradation in spectral performance. Surrounding areas exhibit more favorable resolution values, emphasizing spatial non-uniformity in detector response. This visualization is critical for optimizing crystal geometry and readout positioning in high-precision imaging systems.

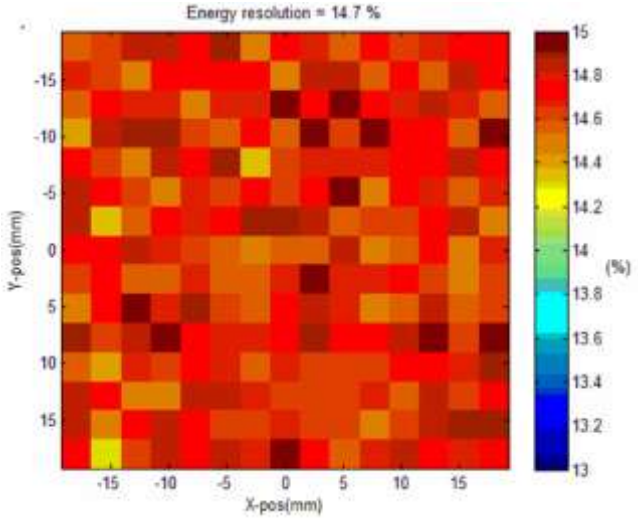

Fig. 18. Energy resolution map for Single-layer block crystals with LYSO 3×3×20 mm3

The spatial ER performance for single-layer block crystals using LYSO with dimensions 3×3×20 mm³ is visualized through a two-dimensional heatmap, as shown in Figure 18. The map spans X and Y positions from approximately −15 mm to 15 mm, with a color gradient indicating ER values ranging from 13.2% (dark blue) to 14.8% (dark red). The central region exhibits slightly elevated resolution values, suggesting localized variations in scintillation response. With an overall ER of 14.7%, this visualization highlights the spatial uniformity and potential optimization areas for enhancing detector performance in high-precision imaging systems.

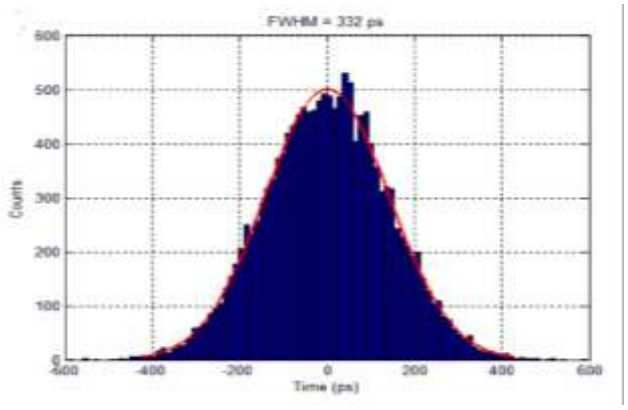

Fig. 19. CTR for Single-layer block crystals with LYSO 3×3×20 mm3

The CTR performance for single-layer block crystals using LYSO with dimensions 3×3×20 mm³ is visualized through a symmetric histogram of photon arrival times, as shown in Figure 19. The blue bars represent measured counts, while the red fitted curve overlays the distribution, capturing the temporal spread of events. A FWHM of 332 ps is reported, indicating moderate timing precision. This result highlights the impact of crystal thickness and configuration on time resolution, offering valuable insights for Time-of-Flight PET and related applications, such as optimizing detector design.

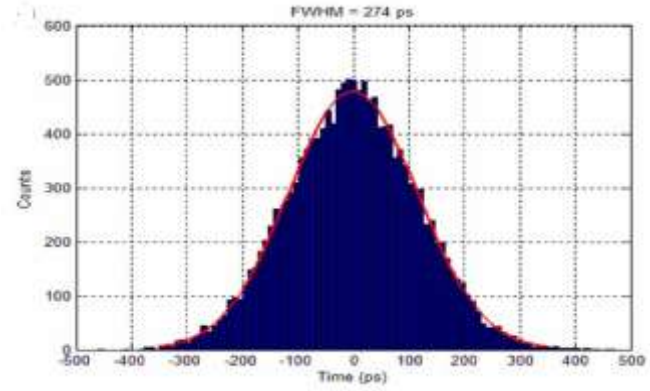

Fig. 20. CTR for Dual-layer block crystals with LYSO 3×3×(8 + 12) mm3

Figure 20 illustrates the CTR performance for dual-layer block crystals composed of LYSO with dimensions 3×3×(8 + 12) mm³, highlighting the system's temporal precision. The histogram shows a symmetric distribution of photon arrival times cantered around zero, with dark blue bars representing the measured counts and a red fitted curve overlaying the data. The FWHM is reported as 274 ps, indicating sub-nanosecond timing resolution. This result underscores the effectiveness of dual-layer crystal configurations in enhancing time-of-flight accuracy for advanced PET imaging and related applications.

10.48047/jocaaa.2024.32.01.72

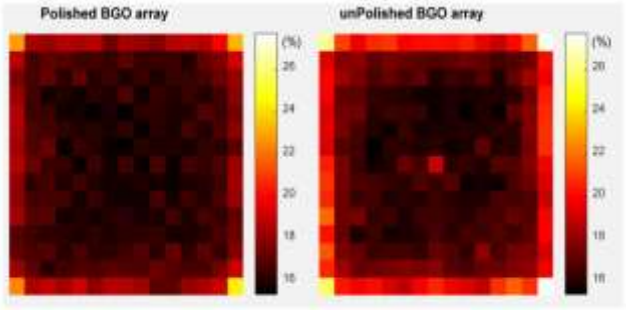

Fig. 21. Energy resolution for the polished and the unpolished BGO array

Figure 21 illustrates the comparative ER performance of polished versus unpolished BGO arrays using heatmap-style visualizations. Each array is represented by a grid of colored cells, where the color intensity corresponds to ER percentages ranging from 16% to 26%. The polished BGO array exhibits a more uniform and higher ER across its elements, predominantly in the yellow-orange range, indicating improved scintillation efficiency and signal consistency. In contrast, the unpolished array shows greater variability and lower resolution values, with darker regions suggesting suboptimal light collection. This visual comparison underscores the enhancement in detector performance achieved through surface polishing.

DOI resolution is critical for accurate 3D localization of gamma-ray interactions, especially in thick or layered crystals where parallax errors can degrade spatial precision. Table X presents a comparative analysis of DOI resolution across various scintillator configurations, highlighting the influence of crystal geometry and material properties on depth sensitivity. The LYSO 1×1×20 mm³ configuration demonstrates the best DOI resolution at 2.33 mm, closely followed by LYSO 0.95×0.95×20 mm³ at 2.81 mm, indicating that fine-pixel LYSO crystals offer superior depth discrimination. LSO arrays show moderate performance with a DOI of 3.68 mm, while unpolished BGO achieves a surprisingly competitive 3.2 mm, significantly outperforming its polished counterpart, which records a poor DOI resolution of 18.4 mm. These results underscore the critical role of surface treatment and crystal design in optimizing DOI performance for PET imaging systems.

TABLE X. COMPARISON OF DOI RESOLUTION ACROSS DIFFERENT SCINTILLATOR CONFIGURATIONS

Configuration	DOI Resolution (mm)
LYSO 0.95×0.95×20[45]	2.81
LSO arrays [46]	3.68
BGO Polished[44]	18.4
BGO Unpolished[44]	3.2
LYSO 1×1 × 20[47]	2.33

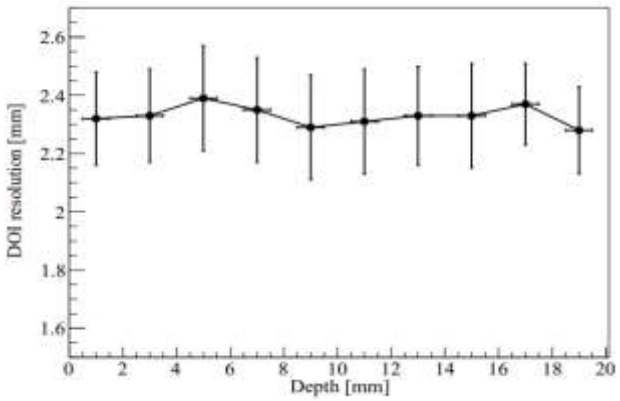

Fig. 22. DOI Resolution for LYSO 1×1 × 20

LYSO scintillator crystal's Depth of Interaction (DOI) resolution profile, as seen in Figure 22, has dimensions of 1×1×20 mm³. The DOI resolution (in mm) against interaction depth, ranging from 0 to 20 mm, with each data point accompanied by vertical error bars to indicate measurement uncertainty. The resolution values remain relatively stable across the depth range, fluctuating between approximately 1.6 mm and 2.6 mm, suggesting consistent DOI performance throughout the crystal length. This uniformity is critical for accurate spatial localization in PET imaging applications, where precise depth discrimination enhances image quality and detector reliability.

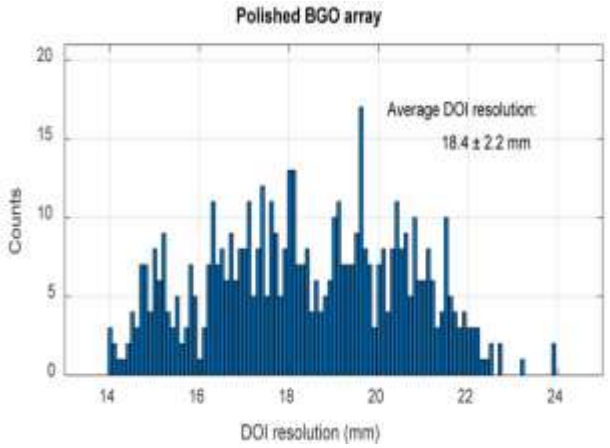

Fig. 23. Distribution of the DOI resolution of polished BGO Array

A polished BGO array's Depth of Interaction (DOI) resolution measurement distribution is shown in Figure 23, highlighting the frequency of counts across a resolution range of 13 to 24 mm. The data reveals a peak concentration around 18–19 mm, indicating the most probable DOI resolution values within the array. An annotated average DOI resolution of 18.4 ± 2.2 mm suggests moderate precision with some variability across detector elements. This performance profile reflects the array's capability for spatial discrimination in radiation detection systems

10.48047/jocaaa.2024.32.01.72

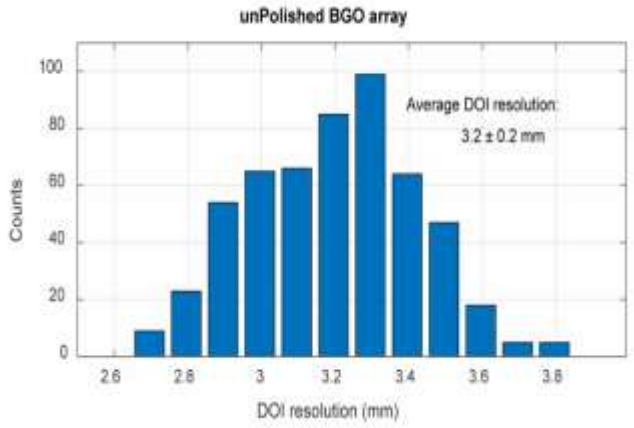

Fig. 24. Distribution of the DOI resolution of unpolished BGO Array

An unfinished BGO array's Depth of Interaction (DOI) resolution measurements are distributed as shown in Figure 24, with a peak centred at 3.2 mm and resolution values ranging from 2.6 to 3.8 mm. The count frequency indicates that most detector elements exhibit DOI resolution near this central value, reflecting relatively consistent performance across the array. An annotated average DOI resolution of 3.2 ± 0.2 mm confirms low variability and tight clustering of measurements, suggesting reliable depth discrimination despite the absence of surface polishing.

A. Comparison and Discussion

This section synthesizes the performance metrics of various PET detector module configurations, focusing on CTR, and ER, capabilities. It critically compares scintillator materials (LYSO, GAGG, BGO, LSO), geometries (cuboid, elongated, layered), and surface treatments (polished vs. unpolished) to identify optimal trade-offs for PET imaging. Table XI presents a comparative evaluation across a range of crystal scintillator configurations, revealing distinct performance trade-offs. LYSO Cuboid exhibits the best CTR at 107 ps with a moderate ER of 11.57%, while GAGG Cuboid offers a strong balance with 114 ps CTR and superior ER of 8.58%. Pixelated LYSO arrays (3×3×15 mm³) and LYSO arrays with fine pitch (3.2 mm & 1.6 mm) also demonstrate excellent timing (≈210 ps) and ER (7–8%). In contrast, monolithic LYSO blocks show degraded performance with 497 ps CTR and 30% energy resolution. BGO polished crystals consistently underperform, with CTR around 3200 ps and ER exceeding 16%, while $BaSO_4$ offers intermediate results. Elongated and layered LYSO formats (e.g., 2.98×20 mm, 3×3×(8+12) mm³) show moderate CTR (180–274 ps) and ER (10.2–13.9%), indicating geometry-dependent trade-offs. Overall, pixelated LYSO and GAGG configurations emerge as optimal for high-resolution PET imaging.

TABLE XI. COMPARISON OF CTR AND ENERGY RESOLUTION ACROSS VARIOUS CRYSTAL SCINTILLATOR CONFIGURATIONS

Configuration	CTR (ps)	Energy Resolution (%)
Monolithic LYSO block (50×50×15 mm³)[48]	497	30
Pixelated LYSO array (8×8, 3×3×15 mm³)[49]	210	7
BGO Polished[44]	3200	17.7
$BaSO_4$ [50]	386	11.07
LYSO 2.98×20 mm[43]	180	10.2
LYSO 1.95×30 mm[43]	263	11.7
BGO Polished[44]	3200	16.9
BGO Unpolished[44]	3500	17.7

Comprehensive evaluation of PET detector modules, offering valuable insights into the impact of scintillator materials, crystal geometries, and readout architectures on imaging performance. By systematically comparing pixelated LYSO, GAGG, BGO, and monolithic designs, it establishes clear benchmarks for CTR, ER, and DOI capabilities. The study highlights the superior performance of pixelated LYSO and GAGG arrays, demonstrating their potential for high-resolution, time-sensitive applications. Overall, the study makes a substantial contribution to the advancement of PET technology by directing the choice of detector configurations that balance precision, efficiency, and clinical relevance particularly for brainPET and organ-specific imaging systems.

X. CONCLUSION AND FUTURE WORK

Positron Emission Tomography (PET) continues to evolve as a cornerstone of functional imaging, with detector module design playing a critical role in advancing resolution, timing, and sensitivity. This comprehensive study examined a wide range of scintillator materials, geometries, and readout configurations to benchmark performance across Coincidence Time Resolution (CTR), Energy Resolution (ER), and Depth of Interaction (DOI) metrics. Pixelated LYSO and GAGG cuboids demonstrated superior performance, achieving CTR in the range of 180–220 ps and ER between 10–12%, while polished BGO and monolithic designs showed limited DOI encoding and timing precision. Dual-layer and staggered arrays improved DOI discrimination and timing uniformity, though they introduced challenges in decoding and fabrication. While pixelated LYSO and GAGG crystals proved effective for high-resolution PET imaging, polished BGO and monolithic blocks though economical and easy to fabricate showed limited DOI encoding and weaker timing performance. To overcome these drawbacks, dual-layer and staggered arrays were introduced, enhancing DOI and timing uniformity but adding decoding and fabrication complexity. This led to simulation-driven optimization decoding for scalable improvements. Future work will focus on validating optimized designs, integrating wavelength-shifting fiber readouts, and developing compact electronics advancing PET systems that balance resolution, manufacturability, and adaptability for brainPET and organ-specific applications.

REFERENCES

[1] E. Yoshida *et al.*, "Basic performance of a large area PET detector with a monolithic scintillator," *Radiol. Phys. Technol.*, 2011, doi: 10.1007/s12194-011-0112-7.

[2] A. J. González *et al.*, "A PET Design Based on SiPM and Monolithic LYSO Crystals: Performance Evaluation," *IEEE Trans. Nucl. Sci.*, 2016, doi: 10.1109/TNS.2016.2522179.

[3] M. Morrocchi *et al.*, "Depth of interaction determination in monolithic scintillator with double side SiPM readout," *EJNMMI Phys.*, 2017, doi: 10.1186/s40658-017-0180-9.

[4] J. J. Vaquero and P. Kinahan, "Positron Emission Tomography: Current Challenges and Opportunities for Technological Advances in Clinical and Preclinical Imaging Systems," *Annu. Rev. Biomed. Eng.*, vol. 17, no. 1, pp. 385–414, Dec. 2015, doi: 10.1146/annurev-bioeng-071114-040723.

[5] G. H. Glover, "Overview of functional magnetic resonance imaging," *Neurosurgery Clinics of North America*. 2011. doi: 10.1016/j.nec.2010.11.001.

[6] A. Kadir *et al.*, "Dynamic changes in PET amyloid and FDG

10.48047/jocaaa.2024.32.01.72

imaging at different stages of Alzheimer's disease," *Neurobiol. Aging*, 2012, doi: 10.1016/j.neurobiolaging.2010.06.015.

[7] K. Herrmann *et al.*, "Evaluation of the genisys4, a bench-top preclinical PET Scanner," *J. Nucl. Med.*, 2013, doi: 10.2967/jnumed.112.114926.

[8] S. Vandenberghe and P. K. Marsden, "PET-MRI: A review of challenges and solutions in the development of integrated multimodality imaging," *Physics in Medicine and Biology*. 2015. doi: 10.1088/0031-9155/60/4/R115.

[9] M. L. James and S. S. Gambhir, "A molecular imaging primer: Modalities, imaging agents, and applications," *Physiological Reviews*. 2012. doi: 10.1152/physrev.00049.2010.

[10] V. Araujo and Esteban, "PET detector technologies for next-generation molecular imaging From single-positron counting to single-photoelectron counting," 2019, doi: https://doi.org/10.4233/uuid:427e3ce3-2b01-4fa0-9e80-bf0e9c033213.

[11] S. Surti and J. S. Karp, "Update on latest advances in time-of-flight PET," *Physica Medica*. 2020. doi: 10.1016/j.ejmp.2020.10.031.

[12] S. Abbaszadeh and C. S. Levin, "New-generation small animal positron emission tomography system for molecular imaging," *J. Med. Imaging*, vol. 4, no. 01, p. 1, Jan. 2017, doi: 10.1117/1.JMI.4.1.011008.

[13] W. W. Moses, "Fundamental limits of spatial resolution in PET," *Nucl. Instruments Methods Phys. Res. Sect. A Accel. Spectrometers, Detect. Assoc. Equip.*, 2011, doi: 10.1016/j.nima.2010.11.092.

[14] J. R. Stickel, J. Qi, and S. R. Cherry, "Fabrication and characterization of a 0.5-mm lutetium oxyorthosilicate detector array for high-resolution PET applications," *J. Nucl. Med.*, 2007.

[15] Y. Shao, X. Sun, K. A. Lan, C. Bircher, K. Lou, and Z. Deng, "Development of a prototype PET scanner with depth-of-interaction measurement using solid-state photomultiplier arrays and parallel readout electronics," *Phys. Med. Biol.*, 2014, doi: 10.1088/0031-9155/59/5/1223.

[16] J. Du, X. Bai, and S. R. Cherry, "Performance comparison of depth-encoding detectors based on dual-ended readout and different SiPMs for high-resolution PET applications," *Phys. Med. Biol.*, 2019, doi: 10.1088/1361-6560/ab1c37.

[17] A. Vandenbroucke, A. M. K. Foudray, P. D. Olcott, and C. S. Levin, "Performance characterization of a new high resolution PET scintillation detector," *Phys. Med. Biol.*, 2010, doi: 10.1088/0031-9155/55/19/018.

[18] S. Vandenberghe, E. Mikhaylova, E. D'Hoe, P. Mollet, and J. S. Karp, "Recent developments in time-of-flight PET," *EJNMMI Phys.*, vol. 3, no. 1, p. 3, Dec. 2016, doi: 10.1186/s40658-016-0138-3.

[19] E. Mikhaylova *et al.*, "Simulation of the expected performance of a seamless scanner for brain pet based on highly pixelated CdTe detectors," *IEEE Trans. Med. Imaging*, 2014, doi: 10.1109/TMI.2013.2284657.

[20] S. T. Abebe, "Simuation And Evaluation of Optical Transparent Ceramic Scintillators Based High-Performance Brain Pet Scanner," Near East University, 2019.

[21] J. Zheng, "Energy metabolism of cancer: Glycolysis versus oxidative phosphorylation (review)," *Oncology Letters*. 2012. doi: 10.3892/ol.2012.928.

[22] S. R. Cherry, J. A. Sorenson, and M. E. Phelps, *Physics in Nuclear Medicine*. 2012. doi: 10.2967/jnumed.113.123125.

[23] P. Gebhardt, J. Wehner, B. Weissler, R. Botnar, P. K. Marsden, and V. Schulz, "FPGA-based RF interference reduction techniques for simultaneous PET-MRI," *Phys. Med. Biol.*, 2016, doi: 10.1088/0031-9155/61/9/3500.

[24] S. España, L. M. Fraile, J. L. Herraiz, J. M. Udías, M. Desco, and J. J. Vaquero, "Performance evaluation of SiPM photodetectors for PET imaging in the presence of magnetic fields," *Nucl. Instruments Methods Phys. Res. Sect. A Accel. Spectrometers, Detect. Assoc. Equip.*, 2010, doi: 10.1016/j.nima.2009.11.066.

[25] H. Zaidi and A. Del Guerra, "An outlook on future design of hybrid PET/MRI systems," *Med. Phys.*, 2011, doi: 10.1118/1.3633909.

[26] J. Cheng-Liao and J. Qi, "Segmentation of mouse dynamic PET images using a multiphase level set method," *Phys. Med. Biol.*, 2010, doi: 10.1088/0031-9155/55/21/014.

[27] A. Baazaoui, W. Barhoumi, E. Zagrouba, and R. Mabrouk, "A Survey of PET Image Segmentation: Applications in Oncology, Cardiology and Neurology," *Curr. Med. Imaging Rev.*, 2015, doi: 10.2174/1573405612666151203204003.

[28] E. Venialgo *et al.*, "PET calibration method of nonlinear position estimation algorithms for continuous NaI(Tl) crystals," in *IEEE Nuclear Science Symposium Conference Record*, 2011. doi: 10.1109/NSSMIC.2011.6152609.

[29] N. Aubry *et al.*, "EndoTOFPET-US: A novel multimodal tool for endoscopy and positron emission tomography," *J. Instrum.*, 2013, doi: 10.1088/1748-0221/8/04/C04002.

[30] G. Llosá *et al.*, "Characterization of a PET detector head based on continuous LYSO crystals and monolithic, 64-pixel silicon photomultiplier matrices," *Phys. Med. Biol.*, 2010, doi: 10.1088/0031-9155/55/23/008.

[31] S. Seifert and D. R. Schaart, "Improving the time resolution of TOF-PET detectors by double-sided readout," *IEEE Trans. Nucl. Sci.*, 2015, doi: 10.1109/TNS.2014.2368932.

[32] P. Peng, S. Subedi, Y. Qiang, H. Hemmati, and S. R. Cherry, "Performance evaluation of a large-area layered structure PET detector module," 2023. doi: 10.1109/nssmicrtsd49126.2023.10337963.

[33] Z. Liu, W. Li, Y. Li, C. Li, X. Wang, and K. Hu, "An FPGA Charge-to-Digital Converter Based on Voltage-Referenced Receivers for PET Applications," *IEEE Trans. Radiat. Plasma Med. Sci.*, 2023, doi: 10.1109/TRPMS.2022.3185216.

[34] H. Kim *et al.*, "A Next Generation Preclinical PET/EPRI: a PET Subsystem Prototype," in *2022 IEEE NSS/MIC RTSD - IEEE Nuclear Science Symposium, Medical Imaging Conference and Room Temperature Semiconductor Detector Conference*, 2022. doi: 10.1109/NSS/MIC44845.2022.10399184.

[35] X. Yu *et al.*, "Requirements of Scintillation Crystals with the Development of PET Scanners," *Crystals*. 2022. doi: 10.3390/cryst12091302.

[36] S. J. Lee and C. H. Baek, "A new method for position determination of scintillation pixel in PET detector module using simulation LUT and MLPE," *Nucl. Instruments Methods Phys. Res. Sect. A Accel. Spectrometers, Detect. Assoc. Equip.*, 2021, doi: 10.1016/j.nima.2021.165750.

[37] C. Zeng *et al.*, "Evaluation of a PET detector based on SiPMs and FPGA-only MVT digitizers," *Nucl. Instruments Methods Phys. Res. Sect. A Accel. Spectrometers, Detect. Assoc. Equip.*, 2021, doi: 10.1016/j.nima.2020.164953.

[38] C. Wu, M. S. Lee, and C. S. Levin, "Neural Network-Based Inter-Crystal Scatter Event Positioning in a PET System Design Based on 3D Position Sensitive Detectors," in *2020 IEEE Nuclear Science Symposium and Medical Imaging Conference, NSS/MIC 2020*, 2020. doi: 10.1109/NSS/MIC42677.2020.9507821.

[39] Z. Deng, Y. Deng, and G. Chen, "Design and evaluation of lyso/sipm lightening pet detector with dti sampling method," *Sensors (Switzerland)*, 2020, doi: 10.3390/s20205820.

[40] S. Lee, K. Y. Kim, and M. S. L. and J. S. Lee, "Performance improvement of GAGG PET by inter-detector and inter-crystal scatter recovery," *J. Nucl. Med.*, vol. 60, no. 1, 2019.

[41] L. Guo, J. Tian, P. Chen, S. E. Derenzo, and W. S. Choong, "Improving timing performance of double-ended readout in TOF-PET detectors," *J. Instrum.*, 2020, doi: 10.1088/1748-0221/15/01/P01003.

[42] H. G. Kang, G. B. Ko, J. T. Rhee, K. M. Kim, J. S. Lee, and S. J. Hong, "A dual-ended readout detector using a meantime method for SiPM TOF-DOI PET," *IEEE Trans. Nucl. Sci.*, 2015, doi: 10.1109/TNS.2015.2449891.

[43] Z. Liu *et al.*, "High resolution detectors for whole-body PET scanners by using dual-ended readout," *EJNMMI Phys.*, 2022, doi: 10.1186/s40658-022-00460-4.

[44] J. Du, "Performance of Dual-Ended Readout PET Detectors Based on BGO Arrays and BaSO Reflector," *IEEE Trans. Radiat. Plasma Med. Sci.*, 2022, doi: 10.1109/TRPMS.2021.3096534.

10.48047/jocaaa.2024.32.01.72

[45] J. Du, X. Bai, and S. R. Cherry, "A depth-of-interaction encoding PET detector module with dual-ended readout using large-area silicon photomultiplier arrays," *Phys. Med. Biol.*, 2018, doi: 10.1088/1361-6560/aaee32.

[46] Y. Yang *et al.*, "A prototype PET scanner with DOI-encoding detectors," *J. Nucl. Med.*, 2008, doi: 10.2967/jnumed.107.049791.

[47] M. Li, Y. Wang, and S. Abbaszadeh, "Development and initial characterization of a high-resolution PET detector module with DOI," *Biomed. Phys. Eng. Express*, 2020, doi: 10.1088/2057-1976/abbd4f.

[48] E. Lamprou, A. J. Gonzalez, F. Sanchez, and J. M. Benlloch, "Exploring TOF capabilities of PET detector blocks based on large monolithic crystals and analog SiPMs," *Phys. Medica*, 2020, doi: 10.1016/j.ejmp.2019.12.004.

[49] H. Leem, Y. Choi, J. Jung, K. Park, Y. Kim, and J. H. Jung, "Optimized TOF-PET detector using scintillation crystal array for brain imaging," *Nucl. Eng. Technol.*, 2022, doi: 10.1016/j.net.2022.02.009.

[50] X. Zhang *et al.*, "Development and Evaluation of a Dual-Layer-Offset PET Detector Constructed with Different Reflectors," *Crystals*, 2022, doi: 10.3390/cryst12010093.